Journal of Materials Processing Tech. 308 (2022) 117708

Contents lists available at ScienceDirect

Journal of Materials Processing Tech.

journal homepage: www.elsevier.com/locate/jmatprotec

Generalized mechanics and dynamics of modulated turning

Bora Eren [a], Soohyun Nam [b], Burak Sencer [a,*]

[a] Oregon State University, Corvallis, USA
[b] Korea Institute of Industrial Technology, the Republic of Korea

ARTICLE INFO

Associate Editor: Erhan Budak

Keywords:
Machining
modulation
vibration
chatter

ABSTRACT

This paper presents a generalized cutting force and regenerative chatter stability prediction for the modulated turning (MT) process. Uncut chip thickness is modeled by considering current tool kinematics and undulated (previously generated) surface topography for any given modulation condition in the feed direction. It is found that chip formation is governed by the undulated surface generated in multiple past spindle rotations. Uncut chip thickness is computed analytically in the form of trigonometric functions, and cutting forces are predicted by making use of orthogonal cutting mechanics. Regenerative chatter stability of the process is also modelled. Analytical semi-discretization-based solution is developed to accurately predict the stability lobe diagrams (SLDs) of the MT process. Predicted stability lobes are validated through numerical time-domain simulations and experimentally via orthogonal (plunge) turning tests. It is found that as compared to conventional single-point continuous turning, regenerative stability of MT exhibits multiple (3) regenerative delay loops and long out-of-cut duration in-between tool engagement stabilizes the process to reach up to 2x higher stable widths/depths as compared to the conventional continuous turning.

1. Introduction

Turning is a well-established and effective material removal process and can provide high material removal rates. A practical problem in turning of ductile materials has been disposal of the cut chips. Long slender chips of ductile material are difficult to break and may cause chip-jam around the cutting point. The most well-known solution for this problem is the use of chip breakers first proposed Zhang and Peklenik (1980). Various mechanical chip breaker strategies have been developed by Jawahir and van Luttervelt (1993). However, robustness of chip breakers among wide range of cutting conditions is limited as shown by Hong et al. (1999). A novel chip guiding system developed by Aoki et al., which does not break the chip but guides it for more efficient chip disposal using a tunnel structure (Aoki et al., 2016). Recently turn-milling process has been employed to prevent chip jam in certain automotive applications that use low carbon steel (Zhu et al., 2015). Turn-milling converts continuous turning into discrete machining to generate short chips like in the milling process. However, it requires relatively expensive multi-purpose machining centers and may suffer from surface location errors when machining cylindrical parts as shown by Uysal et al. (2014). In order to address chip evacuation problem in continuous cutting processes, Low frequency modulation (vibration) assistance has been proposed Mann et al. (2011a) in the past. The first application of low frequency assisted (modulated) machining dates back to 1992 when it was applied in deep hole drilling by Sakurai et al. (1992). This paper focuses on the modulated turning (MT) process and presents a generalized mechanics and dynamics model.

Kinematics of the low frequency MT is illustrated in Fig. 1. As shown, cutting tool is modulated continuously in the feed direction. Such sinusoidal motion generates a wavy surface initially, but for certain modulation amplitudes and frequencies cutting edge loses its contact from the undulated surface. Thus, continuous turning process becomes discrete and generates discontinuous chip, which inherently addresses the chip jam problem. Another advantage of MT is that it does not need special purpose machines since tool modulations are at low frequency and can be realized with the existing drives of a turning center as shown by Chhabra et al. (2002).

Mann et al. (2011a) were the first to analyze kinematics of the MT. They focused on discovering the modulation conditions to generate discrete chip. Fig. 2 illustrates such discrete cutting maps. The shaded areas indicate discrete cutting regions where discontinuous chip is generated. Notice that discrete chip can be generated for a modulation frequency (f_m) of ½ of the spindle rotation frequency (f_s), $f_m = f_s/2$ at a modulation amplitude (A [m]) of ½ of the nominal feed rate (h_0 [m/rev]), $A = h_0/2$. Similar discrete chip generation maps can also be

* Corresponding author.
E-mail address: burak.sencer@oregonstate.edu (B. Sencer).

https://doi.org/10.1016/j.jmatprotec.2022.117708
Received 3 May 2022; Received in revised form 22 June 2022; Accepted 29 June 2022
Available online 5 July 2022

Nomenclature

f_m	Modulation frequency
f_s	Spindle rotation frequency
A	Modulation amplitude [m]
h_0	Nominal feed rate [m]
SS	Spindle speed [min^{-1}]
θ	Spindle rotation angle [rad]
λ	Angular wavelength of tool modulation [rad]
ϕ	Shift in tool trajectories in successive spindle revolutions [rad]
A_{min}	Minimum modulation amplitude for discrete chip generation [m]
y	Tool trajectory [m]
σ	Modulation amplitude and nominal feed rate ratio
γ	Absolute minimum phase difference between tool trajectories [rad]
h	Uncut chip thickness [m]
R_{out}	Air-cutting ratio percentage
h_m	Static uncut chip thickness [m]
h_d	Dynamic uncut chip thickness [m]
τ	Time delay [s]
K_y	Specific cutting force coefficient in feed direction [MPa]
K_x	Specific cutting force coefficient in thrust direction [MPa]
b	Cutting width [m]
F_d	Dynamic cutting force [N]
ΔT	Discretization time step [s]
r	Delay resolution
Φ	State transition matrix
m	Modal mass [kg]
c	Viscous damping coefficient [N/(m•s)]
k	Modal stiffness [N/m]
d	Diameter of workpiece [m]
G_{yy}	Direct dynamic compliance [m/N]
G_{yx}	Cross dynamic compliance [m/N]
G_{eq}	Equivalent dynamic compliance [m/N]
ω_n	Natural frequency [Hz]
a_{lim}	Stability limit of cutting width [m]

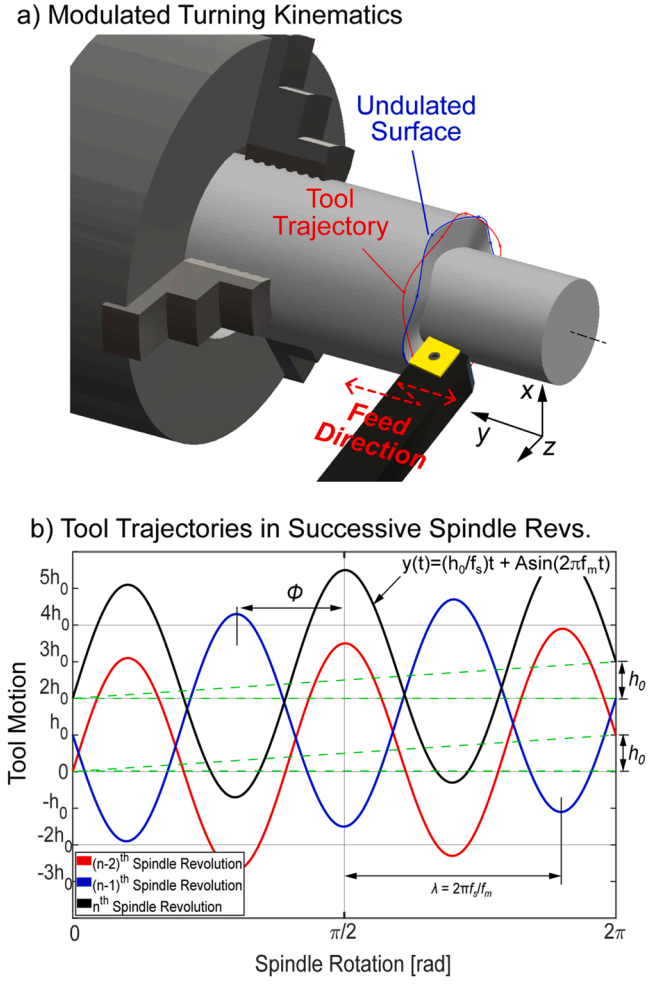

Fig. 1. Kinematics of modulated turning.

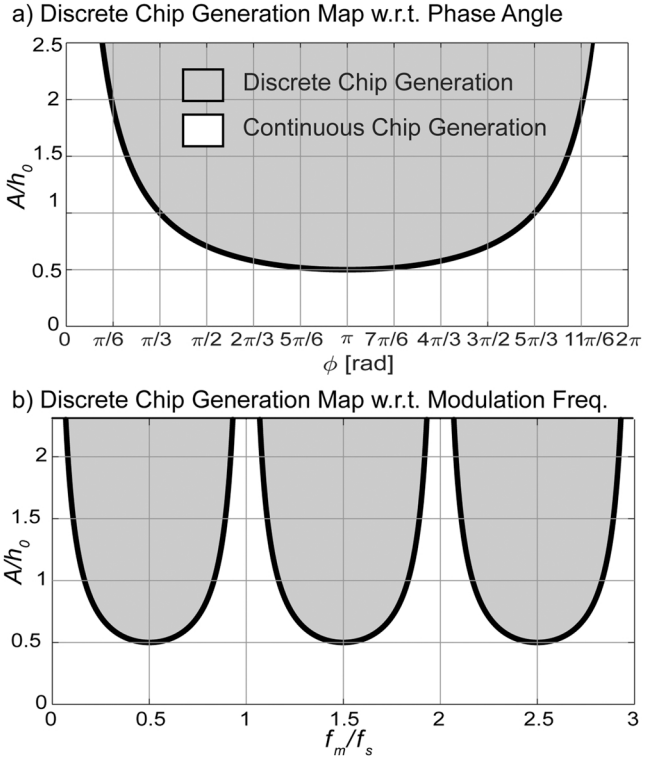

Fig. 2. Discrete chip generation map of modulated turning.

produced for the drilling process by Guo et al. (2017). Notice that when modulation parameters are selected in the discrete cutting zone (gray areas in Fig. 2), tool loses its contact with the workpiece and experiences an air cutting (out-of-cut) phase. Such air-cutting phase is critical for generating discrete chip in machining ductile materials.

Benefits of the low frequency assistance in turning is not limited by just mitigating chip jam as originally proposed. Yeung et al. (2016) analyzed chip formation in modulated turning by synchronous force and

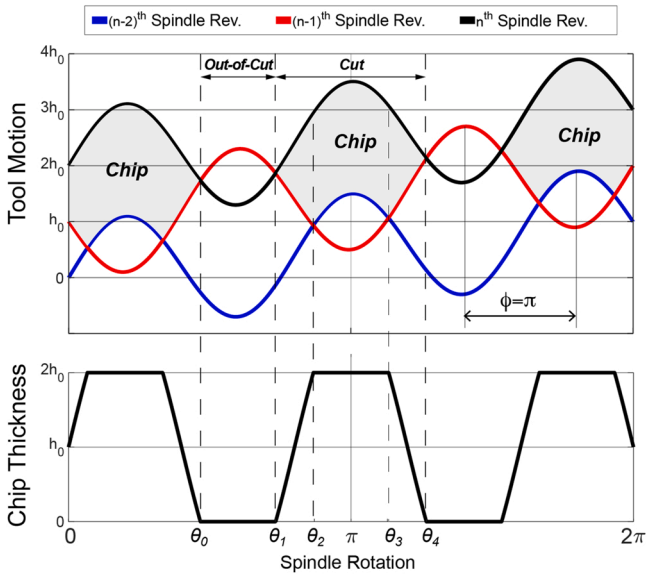

Fig. 3. Tool trajectories and uncut chip thickness for $\phi = \pi$.

image analysis using Particle Image Velocimetry (PIV). They reported that feed modulations can reduce specific cutting energy. Later, Eren and Sencer (2020) have investigated on the specific cutting energy efficiency during modulated turning and concluded that it reduces average cutting effort by utilizing the non-linear relationship between cutting forces and removed material volume. Low frequency tool modulations have potential to reduce average cutting temperature as well. Gao et al. (2016) have measured the temperature distribution in the cutting zone and developed predictive models. They showed that average cutting temperature is lower in modulated turning. Later, Guo et al. have investigated tool-life in modulated machining of compact graphite iron (CGI) workpieces and reported that low frequency feed modulations can significantly improve the tool life (Guo et al., 2012) as compared to continuous cutting.

Dynamics of modulated turning process differs greatly from the conventional continuous turning. Copenhaver et al. (2018) were the first ones to report that tool modulations introduce stabilization effect and helps attain greater chatter stability margins. They used various metrics to detect occurrence of chatter. Notice that in modulated turning, the process is no longer continuous since the cutting tool loses its contact with the workpiece. An air-cutting phase is introduced into the cutting cycle, which in return disturbs development of self-excited chatter vibrations over successive spindle revolutions and helps increase the chatter stability limits. As the average in-cut duration of the tool is minimized, total energy consumed by the dynamic cutting force is reduced. As a result, it increases the gain margin of the process and improves asymptotic chatter stability limits. Multi-axis milling process with complex tool and immersion geometries may provide similar dynamics as reported by Ozkirimli et al. (2016). In turning, such dynamics has been observed in the ultrasonic elliptical vibration cutting (EVC) (Ma et al., 2011). Copenhaver and Schmitz (2020) utilized time-domain simulations to draw stability lobe diagrams (SLDs) of low frequency assisted MT. It was until very recently that Nam et al. proposed a frequency domain-based approach to analytically predict the SLD of MT (Nam et al., 2021). However, the developed frequency domain model could only predict chatter stability when modulation frequency is 0.5, 1.5, 2.5… times of the spindle rotation frequency. It was not general and showed deteriorating accuracy with smaller modulation amplitudes and spindle speeds. This was mainly due to: 1) only 2 delay regeneration effects were included in the modeling stage, and 2) approximations (averaging) used in the derivation of the frequency domain solution.

Based on these past works, this paper provides the following two new knowledge to better understand the kinematics and dynamics of the MT. Firstly, a generalized kinematics model is developed to analytically predict the chip formation and uncut chip thickness. This allows generalized prediction of cutting forces for any set of modulation parameters. Furthermore, it facilitates analytical prediction of cutting duty cycle of the process. Secondly, based on the generalized kinematics, a generalized chatter stability prediction is proposed to accurately predict the regenerative chatter stability for this process. For the first time, it is shown that regenerative chatter stability of modulated turning process is governed by up to 3 regenerative loops leading to a multi-delay regeneration, whereas continuous turning only exhibits single regeneration. In order to accurately predict the SLDs, a semi-discrete time domain model is developed. The proposed model is benchmarked against numerical full time-domain model of the process and validated experimentally in plunge turning tests.

The following sections introduce the generalized kinematics of the process. Chatter stability prediction models are then introduced and validated through simulation studies and in cutting tests.

2. Kinematics of low frequency assisted turning

Fig. 1 illustrates kinematics of MT. As the cutting tool is fed into the workpiece at a nominal feed rate of h_0, sinusoidal modulations (Gao et al., 2018; Mann et al., 2011b) are superimposed as:

$$y(t) = h_0 f_s t + A\sin(2\pi f_m t) \tag{1}$$

where $f_s = 60/SS$ is spindle rotation frequency with spindle speed SS [min^{-1}], f_s is the modulation frequency [Hz], A is the modulation amplitude, and t denotes the time. Eq. (1) can be re-written based on spindle rotation angle θ[rad], and tool trajectory in n^{th} spindle revolution can be expressed as:

$$y_n(\theta) = \left(n-1\right)h_0 + \frac{h_0\theta}{2\pi} + A\sin\left(\frac{2\pi\theta}{\lambda} + \left(n-1\right)\phi\right), \quad 0 \le \theta \le 2\pi \tag{2}$$

where $\lambda = 2\pi f_s/f_m$ [rad] denotes the angular wavelength of tool modulations. Fig. 1b illustrates tool trajectories in successive spindle revolutions. The integer portion of tool modulation-spindle rotation frequency ratio, $\text{int}[f_m/f_s]$ indicates how many full tool modulations are completed within a single spindle revolution, and the phase angle ϕ in 2 (2) is defined based on the remainder as:

$$\phi = 2\pi\left(\frac{f_m}{f_s} - \text{int}\left[\frac{f_m}{f_s}\right]\right), \quad 0 \le \phi \le 2\pi \tag{3}$$

Phase angle ϕ[rad] represents the shift in the tool trajectories in successive spindle revolutions and illustrated in Fig. 3. Setting $0 < \phi < 2\pi$ ensures that there is always an incomplete tool modulation within a single spindle revolution. As a result, tool trajectory continuously shifts ϕ amount over successive spindle rotation, and the tool cuts slightly different angular portion of the workpiece in each spindle revolution. This is the fundamental condition to realize discrete cutting in MT. For any given modulation frequency, ϕmust be determined, and the modulation amplitude, A must be selected to ensure that tool loses its contact with the surface. The minimum modulation amplitude A is determined by ensuring that the n^{th} and $n\text{-}1^{th}$ spindle revolutions, i.e. $y_n(\theta)$ and $y_{n-1}(\theta)$ from 2(2) intersect,

$$y_n(\theta) = y_{n-1}(\theta) \rightarrow A_{\min} = \frac{h_0}{2\sin\left(\frac{\phi}{2}\right)} \tag{4}$$

4(4) reveals that for any phase angle ϕ, there is a minimum modulation amplitude A_{min} that needs to be met for a nominal feed rate, h_0. Note that ϕ is controlled by the ratio f_m/f_s, and Fig. 2 shows the resultant discrete chip generation map also shown by Mann et al. (2011b). For $\phi = \pi$ discrete chip can be generated for the smallest modulation amplitude of $A/h_0 = 0.5$. In the following section chip formation for that most practical condition, i.e. $\phi = \pi$, is firstly analyzed, which is then

Table 1
Chip formation for $\phi = \pi$.

	Phase Angle: $\phi = \pi$				
	θ_1	θ_2	θ_3	θ_4	σ Interval
Tool Trajectory Intersections	$y_n(\theta) \cap y_{n-1}(\theta)$	$y_{n-1}(\theta) \cap y_{n-2}(\theta)$	$y_{n-2}(\theta) \cap y_{n-1}(\theta)$	$y_{n-1}(\theta) \cap y_n(\theta)$	$0.5 \leq \frac{A}{h_0}$

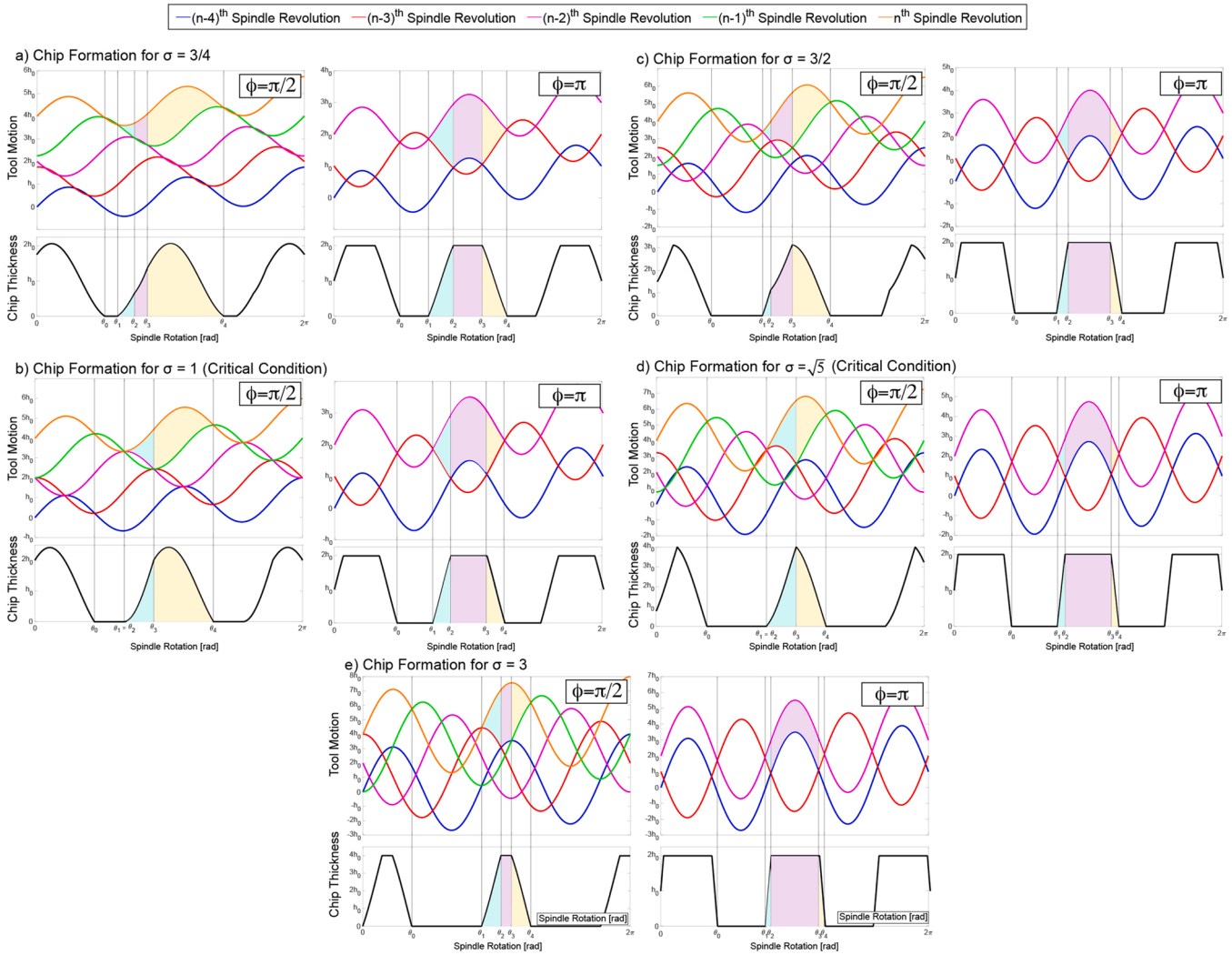

Fig. 4. Comparison of chip formations for different $\sigma = A/h_0$ ratios when $\phi = \pi/2$ and $\phi = \pi$.

followed by the generalized chip formation formulation for any given modulation frequency and amplitude.

2.1. Prediction of chip formation for $\phi = \pi$

Fig. 3 illustrates tool trajectories for $\phi = \pi$ with the light grey shaded areas indicating sections where material is removed, i.e. chip is generated. For $\phi = \pi$, tool modulation is half incomplete within a spindle revolution. This enforces current n^{th} tool trajectory to intersect with the tool trajectories from n-1$^{\text{th}}$ and n-2$^{\text{th}}$ spindle revolutions.

Notice from Fig. 3 that the current (n^{th}) tool trajectory cuts the undulated surface generated by the tool trajectory 2 spindle revolutions before, i.e. n-2$^{\text{th}}$ revolution. Therefore, a single piece of chip is formed within 3 successive, n^{th}, n-1$^{\text{th}}$ and n-2$^{\text{th}}$ revolutions of the spindle. As shown in Fig. 3, a full tool modulation cycle starts with the spindle orientation θ_1 and ends at θ_4. For $\theta \in [\theta_0, \theta_1)$, air cutting is observed, and no chip is generated. For $\theta \in [\theta_1, \theta_2)$ first portion of the chip is formed with the surface generated in the previous n-1$^{\text{th}}$ spindle revolution. While $\theta \in [\theta_2, \theta_3)$ the tool cuts the surface left from the n-2$^{\text{th}}$ spindle revolution. Finally, the last portion of the chip is formed when the tool cuts the surface left from the previous n-1th spindle revolution. Hence, $\theta_1, ., \theta_4$ mark the start and end of each individual segment (portion) of a single piece of chip. Intersection points of the tool trajectories from n^{th} and n-1th spindle revolutions can be used to compute θ_0, θ_1 and θ_4. For instance, tool trajectories in n-1th and n-2$^{\text{th}}$ spindle revolutions intersect with each other to define θ_2 and θ_3, which can be computed using 2(2) as:

Table 2
Chip formation for $\phi = \pi/2$.

	$\phi = \pi/2$					
	θ_1	θ_2	θ_3	θ_4	σ Interval	Row No:
Tool Trajectory Intersections	$y_n(\theta) \cap y_{n-1}(\theta)$	$y_{n-1}(\theta) \cap y_{n-2}(\theta)$	$y_{n-2}(\theta) \cap y_{n-1}(\theta)$	$y_{n-1}(\theta) \cap y_n(\theta)$	$0.7071 \leq \sigma < 1$	1
	$y_n(\theta) \cap y_{n-2}(\theta)$	$y_{n-2}(\theta) \cap y_{n-3}(\theta)$	$y_{n-3}(\theta) \cap y_{n-1}(\theta)$	$y_{n-1}(\theta) \cap y_n(\theta)$	$1 \leq \sigma < 2.236$	2
	$y_n(\theta) \cap y_{n-3}(\theta)$	$y_{n-3}(\theta) \cap y_{n-4}(\theta)$	$y_{n-4}(\theta) \cap y_{n-1}(\theta)$	$y_{n-1}(\theta) \cap y_n(\theta)$	$2.236 \leq \sigma$	3

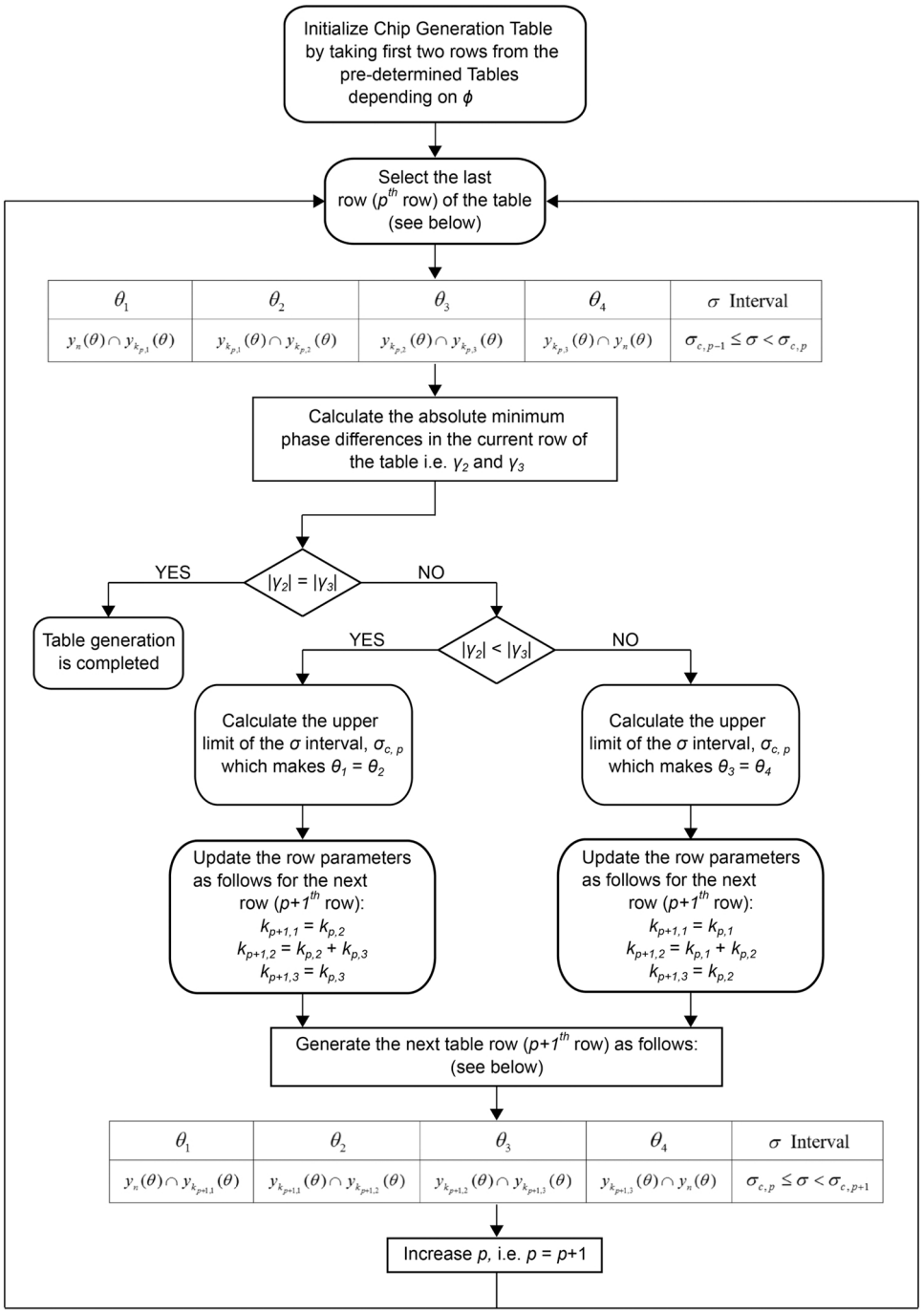

Fig. 5. Flow chart for generating the chip formation table.

Table 3
Initial rows for chip formation for $\phi < \pi$ and $\phi > \pi$.

	$\phi < \pi$					
	θ_1	θ_2	θ_3	θ_4	σ Interval	Row No:
Tool Trajectory Int.	$y_n(\theta) \cap y_{n-1}(\theta)$	$y_{n-1}(\theta) \cap y_{n-2}(\theta)$	$y_{n-2}(\theta) \cap y_{n-1}(\theta)$	$y_{n-1}(\theta) \cap y_n(\theta)$	$\frac{1}{2\sin(\phi/2)} \le \sigma < \sigma_{c,1}$	1
	$y_n(\theta) \cap y_{n-2}(\theta)$	$y_{n-2}(\theta) \cap y_{n-3}(\theta)$	$y_{n-3}(\theta) \cap y_{n-1}(\theta)$	$y_{n-1}(\theta) \cap y_n(\theta)$	$\sigma_{c,1} \le \sigma$	2
	$\phi > \pi$					
	θ_1	θ_2	θ_3	θ_4	σ Interval	Row No:
Tool Trajectory Int.	$y_n(\theta) \cap y_{n-1}(\theta)$	$y_{n-1}(\theta) \cap y_{n-2}(\theta)$	$y_{n-2}(\theta) \cap y_{n-1}(\theta)$	$y_{n-1}(\theta) \cap y_n(\theta)$	$\frac{1}{2\sin(\phi/2)} \le \sigma < \sigma_{c,1}$	1
	$y_n(\theta) \cap y_{n-1}(\theta)$	$y_{n-1}(\theta) \cap y_{n-3}(\theta)$	$y_{n-3}(\theta) \cap y_{n-2}(\theta)$	$y_{n-2}(\theta) \cap y_n(\theta)$	$\sigma_{c,1} \le \sigma$	2

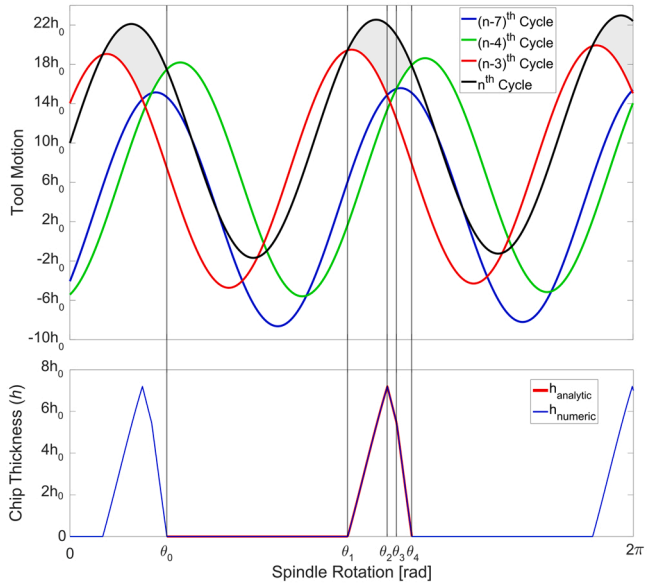

Fig. 6. Tool trajectories and chip formation for $\phi = 108°$.

$$\left.\begin{aligned} \theta_0 &= \frac{\pi + sin^{-1}\left(\frac{h_0}{2A}\right)}{f_m/f_s}, \theta_1 = \frac{2\pi - sin^{-1}\left(\frac{h_0}{2A}\right)}{f_m/f_s} \\ \theta_2 &= \frac{2\pi + sin^{-1}\left(\frac{h_0}{2A}\right)}{f_m/f_s}, \ \theta_3 = \frac{3\pi - sin^{-1}\left(\frac{h_0}{2A}\right)}{f_m/f_s}, \theta_4 = \frac{3\pi + sin^{-1}\left(\frac{h_0}{2A}\right)}{f_m/f_s} \end{aligned}\right\} \tag{5}$$

Above equations can be converted into time domain by setting $t_i = \theta_i/2\pi f_s$, $i = 0.4$, and the ratio of air cutting to cutting within a tool modulation cycle can then be expressed as:

$$\frac{\theta_1 - \theta_0}{\theta_4 - \theta_1} = \frac{\pi - 2\sin^{-1}\left(\frac{h_0}{2A}\right)}{\pi + 2\sin^{-1}\left(\frac{h_0}{2A}\right)} \tag{6}$$

Finally, analytical uncut chip thickness can be derived by simply evaluating the difference between n^{th}, $n\text{-}1^{\text{th}}$ and $n\text{-}2^{\text{th}}$ tool trajectories from 2(2) as:

$$h(t) = \left.\begin{cases} y_n(\theta) - y_{n-1}(\theta), \theta_1 \le \theta < \theta_2 \\ y_n(\theta) - y_{n-2}(\theta), \theta_2 \le \theta < \theta_3 \\ y_n(\theta) - y_{n-1}(\theta), \theta_3 \le \theta \le \theta_4 \end{cases}\right\} \rightarrow \begin{cases} A\left(\sin\left(2\pi\frac{\theta}{\lambda}\right) - \sin\left(2\pi\frac{\theta}{\lambda} + \pi\right)\right) + h_0 \\ 2h_0 \\ A\left(\sin\left(2\pi\frac{\theta}{\lambda}\right) - \sin\left(2\pi\frac{\theta}{\lambda} + \pi\right)\right) + h_0 \end{cases} \tag{7}$$

Above chip formation can also be summarized in a tabulated format shown in Table 1. Each column shows the angular positions of chip segments and which spindle revolutions define them. For instance, chip formation starts at θ_1, and it is generated by the current tool trajectory $y_n(\theta)$ and its intersection with they$_{n-1}(\theta)$ tool trajectory. The next segment (section) of the chip starts at θ_2 defined by the intersection of $y_{n-1}(\theta)$ and $y_{n-2}(\theta)$ tool trajectories. A symmetrical copy of the first chip segment is then observed as a third (last) segment of the chip. The last column of the table indicates for which modulation amplitudes such configuration is valid. For $\phi = \pi$, modulation amplitude does not alter the chip formation. As long as modulation amplitude and nominal feed rate ratio $\sigma = \frac{A}{h_0} \ge 0.5$, discrete chip is always generated by the same tool trajectories. Increasing modulation amplitude, A only increases the air cutting duration and does not alter the maximum uncut chip thickness as indicated in 6(6).

2.2. Prediction of generalized chip formation

To accurately predict the uncut chip thickness for various phase angles and modulation amplitudes, tool trajectories that generate individual sections chip must be identified carefully. This section presents a systematic way to calculate the uncut chip thickness for any given modulation condition.

Firstly, the effect of modulation amplitude on the chip formation is presented through an example. Fig. 4 compares chip generation for phase angles $\phi = \pi/2$ and $\phi = \pi$ at various modulation amplitude and nominal feed rate ratios $\sigma = A/h_0$. As shown, in case of $\phi = \pi/2$ more complex chip formations are generated with changing σ. When σ is small chip formation starts with intersection of n^{th} and $n\text{-}1^{th}$ tool trajectories, then switches to n^{th} and $n\text{-}2^{th}$, and finishes off with n^{th} and $n\text{-}1^{th}$. However, when the modulation amplitude is increased, $\sigma > 1$, chip formation alters. Table 2 provides all the 3 different tool intersections for different modulation amplitudes.

Each column in Table 2 indicates the spindle revolutions involved in chip formation, and each row indicates the chip formation sequence with the increasing modulation amplitude, σ. Notice that 1^{st} row of the Table 2 is identical to the case of $\phi = \pi$ (see Table 1). However, that chip formation it is only valid until $\sigma = 1$. At that upper limit value, multiple (>2) tool trajectories intersect at one point, which is illustrated in Fig. 4b and denoted as the "critical condition". This upper limit value can be solved by setting $\theta_1 = \theta_2$:

$$\left.\begin{aligned} y_n(\theta) &= y_{n-1}(\theta) \rightarrow \theta_1 \\ y_{n-1}(\theta) &= y_{n-2}(\theta) \rightarrow \theta_2 \end{aligned}\right\} \rightarrow \theta_1 = \theta_2 \rightarrow \sigma_{c,\,p=1} \tag{8}$$

where p represents the row number in the table. When σ is further increased, a different chip formation is observed and presented in the 2^{nd} row of Table 2.

It is critical to determine which tool trajectories intersect and form the chip. A generalized approach is developed here to generate the chip formation table for any given modulation condition, and Fig. 5 presents the flow chart to generate the chip formation table automatically. Firstly, for any given phase angle ϕ, the first two rows of the chip formation table are pre-determined; namely, taken from Table 3 based on whether the phase angle is $\phi < \pi$ or $\phi > \pi$. Notice that when $\phi = \pi$, Table 1 is directly used since chip formation does not alter with σ. The remaining chip formations in the chip formation table with the increasing σ (starting from 3rd row) and the upper limit $\sigma_{c,p}$ values of

Table 4
Sample Chip Formation Table for $\phi = 108°$.

	$\phi = 108°$				
	θ_1	θ_2	θ_3	θ_4	σ Interval
Tool Trajectory Intersections	$y_n(\theta) \cap y_{n-1}(\theta)$	$y_{n-1}(\theta) \cap y_{n-2}(\theta)$	$y_{n-2}(\theta) \cap y_{n-1}(\theta)$	$y_{n-1}(\theta) \cap y_n(\theta)$	$0.618 \leq \sigma < 1.0515$
	$y_n(\theta) \cap y_{n-2}(\theta)$	$y_{n-2}(\theta) \cap y_{n-3}(\theta)$	$y_{n-3}(\theta) \cap y_{n-1}(\theta)$	$y_{n-1}(\theta) \cap y_n(\theta)$	$1.0515 \leq \sigma < 5.3405$
	$y_n(\theta) \cap y_{n-3}(\theta)$	$y_{n-3}(\theta) \cap y_{n-4}(\theta)$	$y_{n-4}(\theta) \cap y_{n-1}(\theta)$	$y_{n-1}(\theta) \cap y_n(\theta)$	$5.3405 \leq \sigma < 9.1293$
	$y_n(\theta) \cap y_{n-3}(\theta)$	$y_{n-3}(\theta) \cap y_{n-7}(\theta)$	$y_{n-7}(\theta) \cap y_{n-4}(\theta)$	$y_{n-4}(\theta) \cap y_n(\theta)$	$9.1293 \leq \sigma < 26.3987$
	$y_n(\theta) \cap y_{n-3}(\theta)$	$y_{n-3}(\theta) \cap y_{n-10}(\theta)$	$y_{n-10}(\theta) \cap y_{n-7}(\theta)$	$y_{n-7}(\theta) \cap y_n(\theta)$	$26.3987 \leq \sigma$

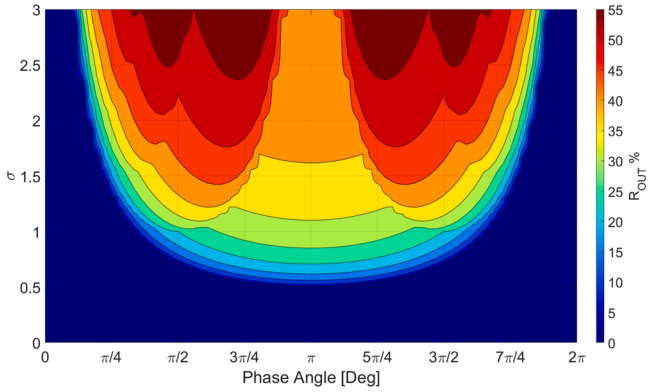

Fig. 7. Cutting duty cycle map $R_{OUT} = \frac{Out-of-cut\ Durtaion}{Total\ Modulation\ Cycle}$.

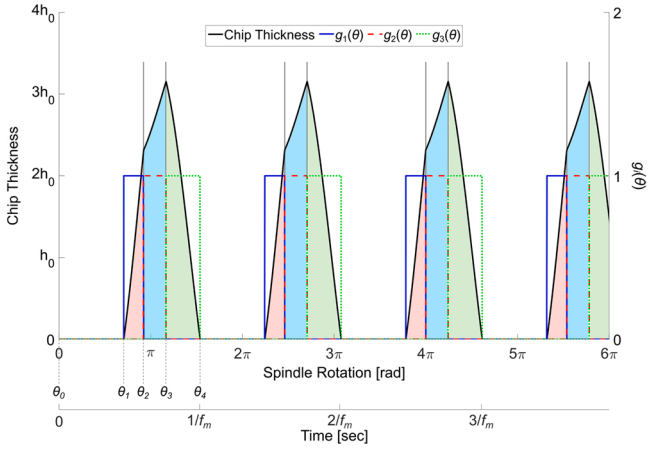

Fig. 8. Periodic unit pulse functions and uncut chip thickness variation.

the rows (starting from 2nd row) are determined by utilizing the flow chart (see Fig. 5). The rest of the chip formation table is created by firstly computing the absolute minimum phase difference γ[rad] between the tool trajectories that determine θ_2 and θ_3 in the previous row by:

$$\gamma = \text{rem}(\phi|\Delta n|, \pi) \tag{9}$$

where *rem* is a function that computes the remainder of the division of $\phi|\Delta n|/\pi$, and Δn is the difference in spindle revolutions. For instance, consider the case of $\phi = \pi/2$ in Table 2, and observe the chip formation in the 2nd row. Phase difference between the tool trajectories that determine θ_2 is calculated as $\gamma_2 = \text{rem}(\frac{\pi}{2}|(n-2) - (n-3)|, \pi)$, and for θ_3, it becomes $\gamma_3 = \text{rem}(\frac{\pi}{2}|(n-3) - (n-1)|, \pi)$. It should be noted that γ must be converted to stay within the bounds of $-\pi < \gamma < \pi$ Based on the γ value, upper limit of the modulation amplitude $\sigma_{c,p}$ is determined by the mutual intersection point of tool trajectories θ_1 and θ_2 or θ_3 and θ_4. In other words, a unique $\sigma_{c,p}$ value which makes $\theta_1 = \theta_2$ or $\theta_3 = \theta_4$ must be found for the current row of the table. As given in the flow chart, a new row is then added that describes the new chip formation when the modulation amplitude is further increased, $\sigma > \sigma_{c,p}$. Spindle modulations that determine this new chip formation are determined as presented in the flow chart.

By following the flow chart in Fig. 5, all the possible chip formations can be determined. Specifically, spindle revolutions that form various sections of the chip are deduced.

2.3. Illustrative Example

An illustrative example is provided in Fig. 6 to showcase how the tabulated approach can predict complex chip formations in modulated turning. In the example, the phase angle is set to $\phi = 108°$. Table 4 is generated by following the flow chart given in Fig. 5. As shown, with the increasing modulation amplitude σ, there are 5 different chip formations. An example of tool trajectories and resultant chip formation is provided for the 4th row of the Table 4. As illustrated, chip generation starts with the intersection of the tool trajectories of n^{th} and n-3^{th} spindle revolutions. Subsequently, tool trajectory in n-3^{th} spindle revolution intersects with n-7^{th} revolution This initiates generation of the second segment of the chip. Next, tool trajectory in n-7^{th} revolution intersects with the n-4^{th} to form the third segment of the chip. Finally, n-4^{th} trajectory intersects with the current n^{th} tool trajectory. As a result, the chip has 3 different sections where the first chip portion is formed with the undulated surface generated 3 spindle revolutions before. The second chip portion is formed with surface cut 7 revolutions before, and the last portion is generated with the surface formed 4 revolutions before. The uncut chip thickness can be computed analytically by using the entries in the table, and the tool trajectory expression given in 2(2). It can also be simulated numerically by calculating the difference between the current tool trajectory and the maximum of past ones as $h(\theta) = y_n(\theta) - \max\{y_{n-1}(\theta), y_{n-2}(\theta), ., y_1\}$. Fig. 6 shows that the simulated and analytically computed uncut chip thicknesses match well.

Finally, air cutting duration for various modulation amplitudes and frequencies can be predicted. Fig. 7 is generated using the proposed generalized chip formation approach and predicts the air-cutting ratio percentage $\left(R_{OUT}\% = \frac{\theta_1 - \theta_0}{\theta_4 - \theta_0} \times 100\right)$ for all the possible modulation frequencies, feed rates and amplitudes. As shown, the largest air cutting is achieved when $\phi \cong \pi/2$ or $\phi \cong 3\pi/2$ is selected. Overall, by utilizing the proposed map, modulation parameters can be tuned accurately to achieve more robust discrete chip generation and higher stability.

3. Prediction of regenerative chatter stability

3.1. Semi-discrete time domain solution

Previous section presented that a single discrete chip generated in modulated turning (MT) has 3 portions (sections). Each chip portion is formed by the tool trajectory in the current (n^{th}) spindle revolution and with the undulated surface generated in past spindle revolutions (see Fig. 4). When machining with a flexible workpiece/tool system, cutting forces excite the mechanical structure and introduce a dynamic chip formation component. The total uncut chip thickness can be expressed by:

$$h(\theta) = h_m(\theta) + h_d(\theta) = \underbrace{y_n(\theta) - \max\left\{y_{n-1}(\theta), y_{n-2}(\theta), ., y_{n-(lcm(\phi,2\pi)/\phi)}\right\}}_{h_m} + \underbrace{\left\{\begin{array}{l} -g_{cut}(\theta)y_d(\theta)+g_1(\theta)y_d(\theta-2\pi d_1) \\ +g_2(\theta)y_d(\theta-2\pi d_2)+g_3(\theta)y_d(\theta-2\pi d_3)\end{array}\right\}}_{h_d} \tag{10}$$

h_m [m] is the commanded (static) uncut chip thickness, which is dictated by the low frequency rigid body motion of the tool where *lcm* calculates the least common multiple, and h_d [m] is the dynamic chip component generated by the structural vibrations of the tool/workpiece between present n^{th} and 3 past spindle revolutions; namely, n-d_1, n-d_2 and n-d_3. $d_{j=1,2,3}$ denotes the spindle revolution counter that can be determined for any given modulation amplitude feedrate ratio σ and the phase angle ϕ based on the tabulated approach presented in previous section. $g_{cut}(\theta)$ is a unit pulse (windowing) function periodic at the modulation frequency f_m activated only when the tool is in-cut, i.e. immersed into the workpiece. $g_{j=1,2,3}(\theta)$ denotes set of another periodic unit pulse functions that are activated based on the individual segments of the dynamic uncut chip thickness that is formed between current and past tool vibrations. For example, $g_1(\theta)$ indicates formation of the first chip segment. Similarly, $g_2(\theta)$ and $g_3(\theta)$ are activated when the second and third portions/segments of the chip are formed. Fig. 8 illustrates definition of these windowing functions expressed as:

$$\begin{aligned} g_{cut}(\theta) &= \begin{cases} 1, & \theta_1 \le \text{mod}(\theta, 2\pi) \le \theta_4 \\ 0, & \text{elsewhere} \end{cases} \\ g_1(\theta) &= \begin{cases} 1, & \theta_1 \le \text{mod}(\theta, 2\pi) < \theta_2 \\ 0, & \text{elsewhere} \end{cases} \\ g_2(\theta) &= \begin{cases} 1, & \theta_2 \le \text{mod}(\theta, 2\pi) < \theta_3 \\ 0, & \text{elsewhere} \end{cases} \\ g_3(\theta) &= \begin{cases} 1, & \theta_3 \le \text{mod}(\theta, 2\pi) \le \theta_4 \\ 0, & \text{elsewhere} \end{cases} \end{aligned} \tag{11}$$

where $\theta_1, \ldots, \theta_4$ indicate the start and end of individual chip portions. Since the modulation frequency is typically much lower than the resonance frequencies of the flexible tool/workpiece structure, static uncut chip thickness component h_m in 10(10) does not affect growth of chatter vibrations and can be dropped. Noting that $\theta = 2\pi f_s t$, 10(10) is re-written in time domain as:

$$h_d(t) = -g_{cut}(t)y(t) + g_1(t)y(t-\tau_1) + g_2(t)y(t-\tau_2) + g_3(t)y(t-\tau_3) \tag{12}$$

where $\tau_j = d_j/f_s$ [s] are the time delays originating by the dynamic uncut chip thickness formed by the current and 3 past tool vibrations, $j = 1,2,3$. Please note that those 3 past tool vibrations (regenerations) can originate from multiple spindle revolutions. As an example, Fig. 6 shows that for $\phi = 108^\circ$ when $9.1293 \le \sigma < 26.3987$, regeneration delays would originate from 3, 7 and 4 spindle revolutions before. The table generation procedure presented in Section 2 must be followed to accurately determine the chip formation and the delays.

Workpiece/tool dynamics is approximated by a single degree of freedom (SDOF) system in the feed direction and the equation of motion for the process can be expressed by:

$$\begin{aligned} m_y\ddot{y}_d(t) + c_y\dot{y}_d(t) + k_y y_d(t) = F_d(t) &= K_y b h_d(t) \\ &= K_y b \left\{\begin{array}{l} -g_{cut}(t)y_d(t) + g_1(t)y_d(t-\tau_1) \\ +g_2(t)y_d(t-\tau_2) + g_3(t)y_d(t-\tau_3)\end{array}\right\} \end{aligned} \tag{13}$$

where the K_y [MPa] is the specific cutting force coefficient in the feed direction, b [m] is the cutting width, and F_d [N] becomes the dynamic cutting force. Since the right hand side of 13(13) includes time varying periodic windowing functions and depends on the 3 past vibration states, dynamics of the modulated turning process is represented by a time-varying delay differential equation with multiple delay terms as opposed to conventional turning or milling process dynamics that typically modeled by a single delay and time-invariant as shown by Altintas (2011).

Stability of modulated turning with multiple delays is firstly analyzed in discrete time domain by applying the semi-discrete technique presented by Insperger and Stépán (2004). Dynamics of the orthogonal cutting system from 13(13) is put in a state-space form with 2 states, $x_1(t) = y_d(t)$ and $x_2(t) = dy_d(t)/dt$where

$$\begin{aligned} \frac{d^2y_d(t)}{dt^2} &= \frac{dx_2(t)}{dt} \\ &= -\omega_n^2\left(1 + g_{cut}(t)\frac{K_y b}{k_y}\right)x_1(t) - 2\zeta\omega_n x_2(t) + \frac{\omega_n^2}{k_x}K_y b\begin{bmatrix} g_1(t)x_1(t-\tau_1) \\ +g_2(t)x_1(t-\tau_2) \\ +g_3(t)x_1(t-\tau_3)\end{bmatrix} \end{aligned} \tag{14}$$

and expressed as set of first order differential equations:

$$\begin{aligned} \underbrace{\begin{Bmatrix} \dot{x}_1(t) \\ \dot{x}_2(t)\end{Bmatrix}}_{\dot{\mathbf{x}}(t)} &= \underbrace{\begin{bmatrix} 0 & 1 \\ -\omega_n^2\left(1 + g_{cut}(t)\frac{K_y b}{k_y}\right) & -2\zeta\omega_n\end{bmatrix}}_{\mathbf{A}(t)}\underbrace{\begin{Bmatrix} x_1(t) \\ x_2(t)\end{Bmatrix}}_{\mathbf{x}(t)} + \underbrace{\begin{bmatrix} 0 & 0 \\ \frac{\omega_n^2}{k_y}K_y b g_1(t) & 0\end{bmatrix}}_{\mathbf{B}_1(t)}\underbrace{\begin{Bmatrix} x_1(t-\tau_1) \\ 0\end{Bmatrix}}_{\mathbf{x}(t-\tau_1)} + \\ &\underbrace{\begin{bmatrix} 0 & 0 \\ \frac{\omega_n^2}{k_y}K_y b g_2(t) & 0\end{bmatrix}}_{\mathbf{B}_2(t)}\underbrace{\begin{Bmatrix} x_1(t-\tau_2) \\ 0\end{Bmatrix}}_{\mathbf{x}(t-\tau_2)} + \underbrace{\begin{bmatrix} 0 & 0 \\ \frac{\omega_n^2}{k_y}K_y b g_3(t) & 0\end{bmatrix}}_{\mathbf{B}_3(t)}\underbrace{\begin{Bmatrix} x_1(t-\tau_3) \\ 0\end{Bmatrix}}_{\mathbf{x}(t-\tau_3)} \end{aligned} \tag{15}$$

$$\dot{\mathbf{x}}(t) = \mathbf{A}(t)\mathbf{x}(t) + \sum_{j=1}^{3}\mathbf{B}_j(t)\mathbf{x}(t-\tau_j)$$

In the above state-space representation (15(15)), delayed states are used as forcing functions (inputs) rather than the states of the system. 15(15) is then discretized:

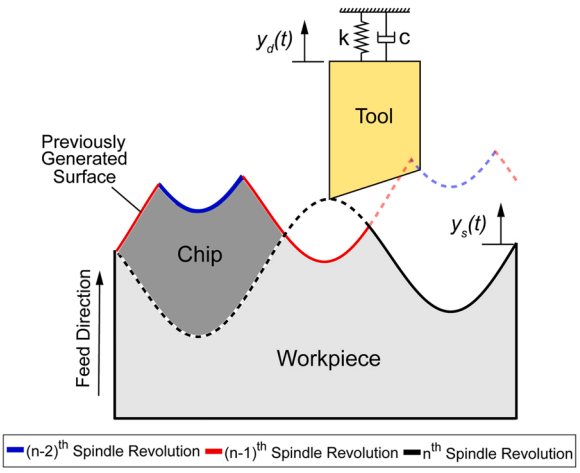

Fig. 9. Time domain simulation model.

$$\dot{\mathbf{x}}(t) = \mathbf{A}_i\mathbf{x}(t) + \sum_{j=1}^{3}\mathbf{B}_{j,i}\mathbf{x}\left(t-\tau_j\right), \quad t \in [t_i, t_{i+1}) \tag{16}$$

where $t_i = i\Delta T$ [s] is the discrete (sampled) time with a discretization time step of ΔT[s], which is selected as follows. The windowing functions are periodic by the modulation cycle, $1/f_m$, and the delay period of the system is dictated by the largest delay $\max(\tau_{j=1,2,3})$. Delay resolution r must be selected large enough to capture both chatter and modulation frequencies. For $r \in \mathbb{Z}^+$, the discretization time step becomes $\Delta T = \min(\tau_{j=1,2,3})/r$.

The delayed states in 16(16) are approximated by their average over two successive samples:

$$\mathbf{x}\left(t_i-\tau_j\right) \approx \frac{1}{2}\left(\mathbf{x}_{i-r_j+1} + \mathbf{x}_{i-r_j}\right) \tag{17}$$

where $r_j = \text{int}(\tau_j/\Delta T)$ is the delay samples for the delayed states. Similarly, the continuous time-varying state transition $\mathbf{A}(t)$ and input $\mathbf{B}_j(t)$ matrices (See 16(16)) can be discretized by taking their average over a sampling interval as shown by Insperger and Stépán (2004),

$$\left.\begin{aligned}\mathbf{A}_i &= \frac{1}{\Delta T}\int_{t_i}^{t_{i+1}}\mathbf{A}(t)dt \\ \mathbf{B}_{j,i} &= \frac{1}{\Delta T}\int_{t_i}^{t_{i+1}}\mathbf{B}_j(t)dt, j = 1,2,3\end{aligned}\right\} \tag{18}$$

and 16(16) is written over the interval $[t_i, t_{i+1})$ as:

$$\mathbf{x}_{i+1} = \mathbf{L}_i\mathbf{x}_i + \frac{1}{2}\sum_{j=1}^{3}\mathbf{R}_{j,i}\left(\mathbf{x}_{i-r_j+1} + \mathbf{x}_{i-r_j}\right) \tag{19}$$

where

$$\left.\begin{aligned}\mathbf{L}_i &= e^{\mathbf{A}_i\Delta T} \\ \mathbf{R}_{j,i} &= \int_0^{\Delta T} e^{\mathbf{A}_i(\Delta T-s)}ds\ \mathbf{B}_{j,i}\end{aligned}\right\} \tag{20}$$

If $\mathbf{A}_i^{-1}$ exists, then the integration in 20(20) gives

$$\mathbf{R}_{j,i} = \left(e^{\mathbf{A}_i\Delta T} - \mathbf{I}\right)\mathbf{A}_i^{-1}\mathbf{B}_{j,i} \tag{21}$$

where $\mathbf{I}$ is a 2×2 identity matrix. Finally, by assuming $r_3 > r_2 > r_1$, 19(19) can be written in matrix-vector from as

$$\mathbf{z}_{i+1} = \boldsymbol{\Phi}_i\mathbf{z}_i \tag{22}$$

where

$$\mathbf{z}_i = \left(\mathbf{x}_i, \mathbf{x}_{i-1}\ldots\mathbf{x}_{i-r_1+1}, \mathbf{x}_{i-r_1}\ldots\mathbf{x}_{i-r_2+1}, \mathbf{x}_{i-r_2}\ldots\mathbf{x}_{i-r_3+1}, \mathbf{x}_{i-r_3}\right)^T \tag{23}$$

Finally, the augmented state transition matrix $\boldsymbol{\Phi}_i$ is constructed as:

$$\boldsymbol{\Phi}_i = \begin{bmatrix} \mathbf{L}_i & \mathbf{0} & \cdots & \mathbf{0} & \mathbf{0} \\ \mathbf{I} & \mathbf{0} & \cdots & \mathbf{0} & \mathbf{0} \\ \mathbf{0} & \mathbf{I} & \cdots & \mathbf{0} & \mathbf{0} \\ \vdots & & \ddots & & \vdots \\ \mathbf{0} & \mathbf{0} & \cdots & \mathbf{I} & \mathbf{0} \end{bmatrix}_{2(\max(r_j)+1)\times 2(\max(r_j)+1)} + \sum_{j=1}^{3}\begin{bmatrix} & & & & \overset{1}{\downarrow} & & & & \\ & & & & & & & & \overset{r_j}{\downarrow} \\ & & & & & & & & \overset{r_j+1}{\downarrow} \\ 0 & 0 & \cdots & 0 & \frac{1}{2}R_{j,i} & \frac{1}{2}R_{j,i} & 0 & \cdots & 0 \\ 0 & 0 & \cdots & 0 & 0 & 0 & 0 & \cdots & 0 \\ 0 & 0 & \cdots & 0 & 0 & 0 & 0 & \cdots & 0 \\ \vdots & \vdots & & \vdots & \vdots & \vdots & \vdots & & \vdots \\ 0 & 0 & \cdots & 0 & 0 & 0 & 0 & \cdots & 0 \end{bmatrix}_{2(\max(r_j)+1)\times 2(\max(r_j)+1)} \tag{24}$$

The discrete state transition matrix $\boldsymbol{\Phi}_i$ is time varying, and it needs to be evaluated based on 20(20) at each sample. Time varying dynamics of the process can be simulated by solving the discrete set of recursive equations from 22(22). The stability of the overall system can be evaluated through $q = \text{int}\left(\frac{1}{\Delta T f_m}\right)$ times repeated application of 22(22):

$$\mathbf{z}_{i+q} = \overline{\boldsymbol{\Phi}}\,\mathbf{z}_i = \boldsymbol{\Phi}_{i+q-1}\boldsymbol{\Phi}_{i+q-2}\cdots\boldsymbol{\Phi}_i\,\mathbf{z}_i \tag{25}$$

According to the Floquet theory (Altintas et al., 2008; Insperger and Stépán, 2004), stability of the linear system described by 25(25) can be tested by evaluating eigenvalues λ of the final state transition matrix $\overline{\boldsymbol{\Phi}}$ as:

$$\mathbf{z}_{i+q} = \overline{\boldsymbol{\Phi}}\,\mathbf{z}_i \rightarrow |\lambda\mathbf{I} - \overline{\boldsymbol{\Phi}}| = 0 \tag{26}$$

Based on the calculated eigenvalues, if $|\lambda| < 1$ the system will be stable exhibiting only forced vibrations. If $|\lambda| > 1$ the system is unstable and leads to regenerative chatter vibrations. If $|\lambda| = 1$, the system would be critically stable. Henceforth, stability lobes diagrams (SLD) can be constructed analytically by scanning the spindle speed at the operating range of the machine at discrete increments and increasing the width of cut at acceptable increments Δb for any given set of modulation parameters; namely, modulation amplitude and feed rate ratio σ, and the phase angle ϕ.

Table 5
Identified specific cutting coefficients.

Specific Cutting Force Coefficient	Calculated Value
K_y(feed)	1338 [N/mm^2]
K_x(principal)	1537 [N/mm^2]

Table 6
Identified dynamic system parameters of the experimental setup.

Dynamic System Parameters	
Natural Frequency (ω_n)	2.55 [kHz]
Mass (m)	0.05 [kg]
Viscous Damping Coefficient (c)	49.31 [N/m/s]
Stiffness (k)	1.45×10^7 [N/m]

3.2. Time domain simulation of the process dynamics

To benchmark accuracy of the presented analytical stability solution, dynamics of the process is also simulated in time domain. The discrete time domain simulation technique presented by (Copenhaver and Schmitz, 2020) is adapted here with minor modifications and briefly summarized in the following.

The simulation model is illustrated in Fig. 9. As shown, structural flexibility is assigned to the tool side, and it is modeled as a SDOF system where $u(t)$ denotes the dynamic displacement of the tool tip. In modulated turning, the tool modulation frequency is significantly lower than any of the structural resonances of the machining system. Therefore, the interaction between rigid body tool motion and flexible structural dynamics can be considered negligible. This assumption is realized by feeding a modulated workpiece surface to the tool rather than directly modulating the tool itself as:

$$y_s(t_i) = f_s h_0 t_i + A\sin(2\pi f_m t_i) \tag{27}$$

Note that the discretization interval ΔT should be selected small enough to capture chatter vibrations. The relative dynamic displacement between the tool tip and workpiece surface is expressed as:

$$u(t_i) = y_s(t_i) - y_d(t_i) \tag{28}$$

and registered in the memory so that the workpiece surface can be updated over N spindle revolutions, and uncut chip thickness due to

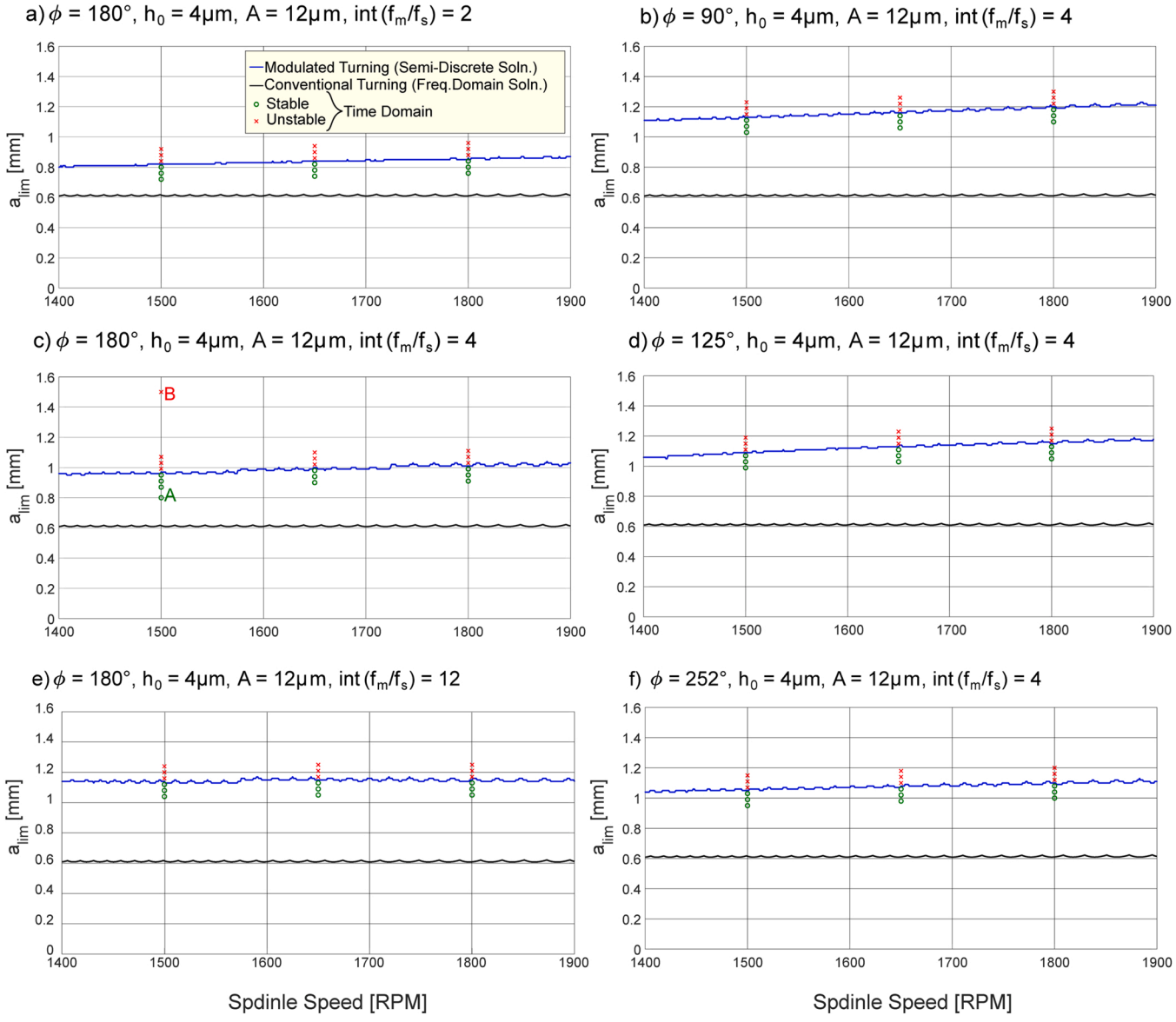

Fig. 10. Benchmark of semi-discrete and time domain stability solutions.

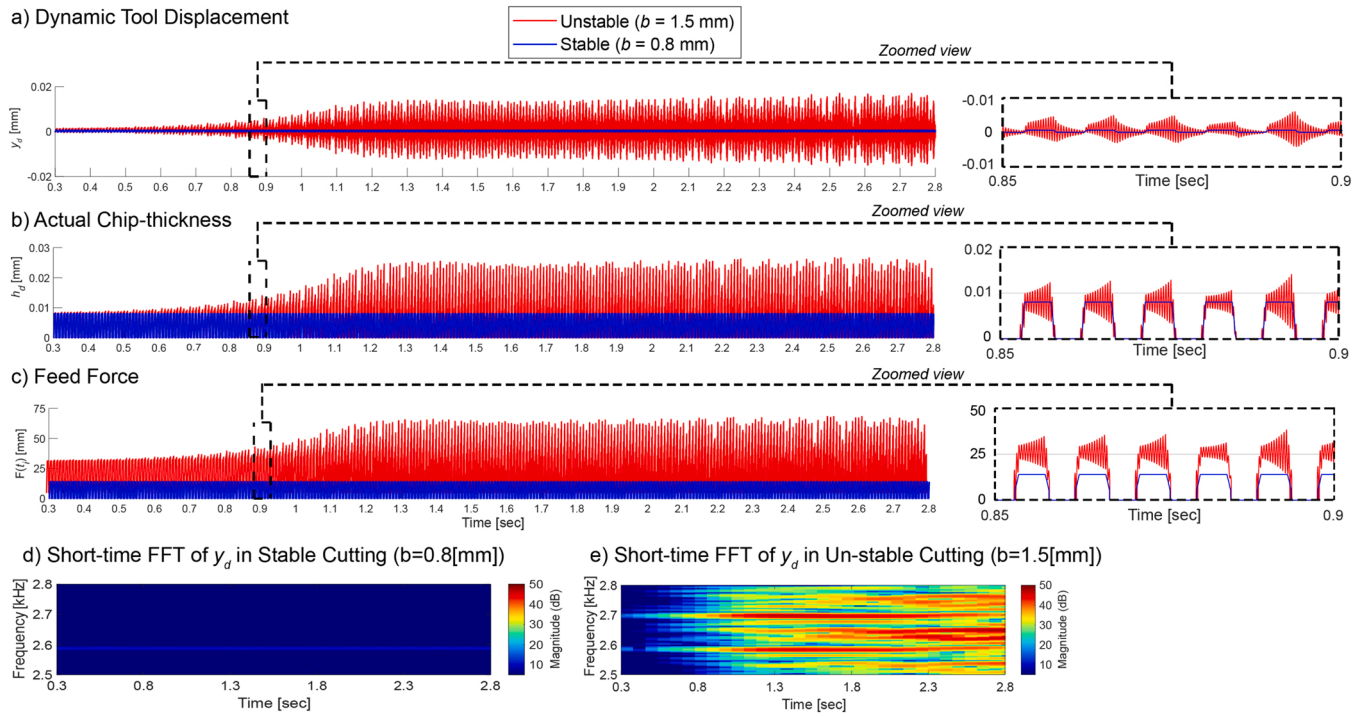

Fig. 11. Time domain simulation of stable and unstable conditions for $\phi = \pi$, $h_0 = 4\mu m$, $A = 12\mu m$, $\text{int}(f_m/f_s) = 4$, $f_s = 25\ Hz$, $f_m = 112.5\ Hz$ at $b_{unstable} = 1.5\ mm$, $b_{stable} = 0.8\ mm$.

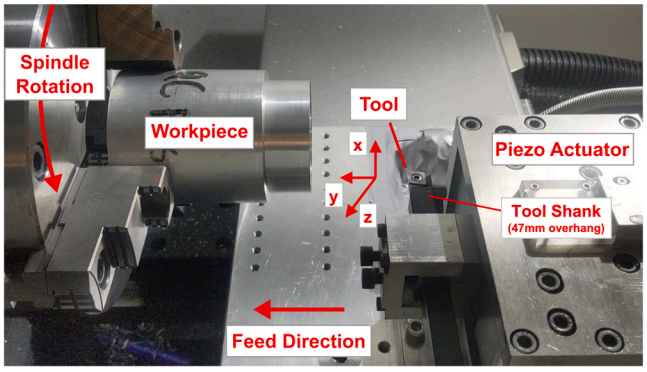

Fig. 12. Experimental setup.

undulated workpiece surface is computed as follows:

$$h_d(t_i) = u(t_i) - \max\left\{u\left(t_i - \frac{1}{f_s}\right), u\left(t_i - \frac{2}{f_s}\right), ., u\left(t_i - \frac{N}{f_s}\right)\right\} \tag{29}$$

Notice that 29(29) allows direct evaluation of the actual dynamic uncut chip thickness and eliminates the need to use any windowing functions. Cutting force is generated when the dynamic uncut chip thickness is positive $h(t_i) > 0$,

$$F(t_i) = \begin{cases} K_y b h(t_i)\ , & h(t_i) > 0 \\ 0 & , \text{else} \end{cases} \tag{30}$$

This allows incorporating tool's jump out of the cut jumping phenomenon (Dombovari et al., 2017), which cannot be simulated by the semi-discrete domain approach. Cutting force generated by the dynamic tool tip displacement can then be expressed as

$$m\ddot{y}_d(t_i) + c\dot{y}_d(t_i) + k y_d(t_i) = F(t_i) \tag{31}$$

where m[kg], c[N/(m•s)], k[N/m] represent mass, viscous damping coefficient and stiffness respectively and 31(31) is digitized by

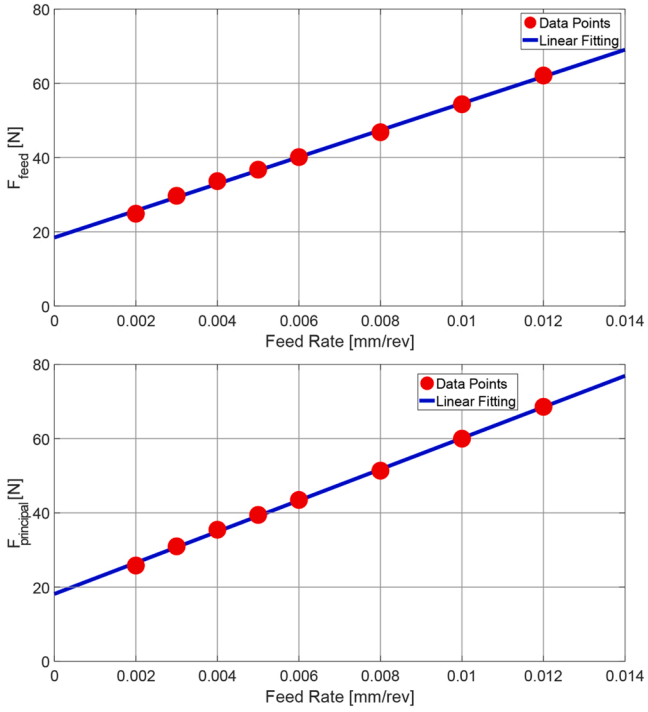

Fig. 13. Specific cutting force identification for orthogonal cutting of Al6061 T6511 tube with $b = 2.75$ [mm].

approximating higher order derivatives of the tool displacement $u(t_i)$ based on second order central differentiation by

$$\left.\begin{aligned} \dot{y}_d(t_i) &= \frac{y_d(t_{i+1}) - y_d(t_{i-1})}{2\Delta T} \\ \ddot{y}_d(t_i) &= \frac{y_d(t_{i+1}) - 2y_d(t_i) + y_d(t_{i-1})}{\Delta T^2} \end{aligned}\right\} \tag{32}$$

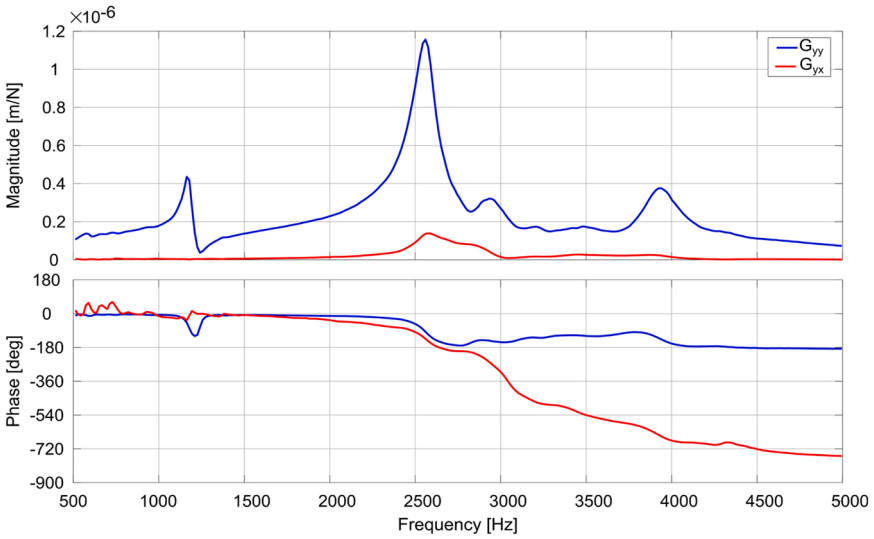

Fig. 14. Direct (G_{yy}) and cross (G_{yx}) dynamic compliance of the tool.

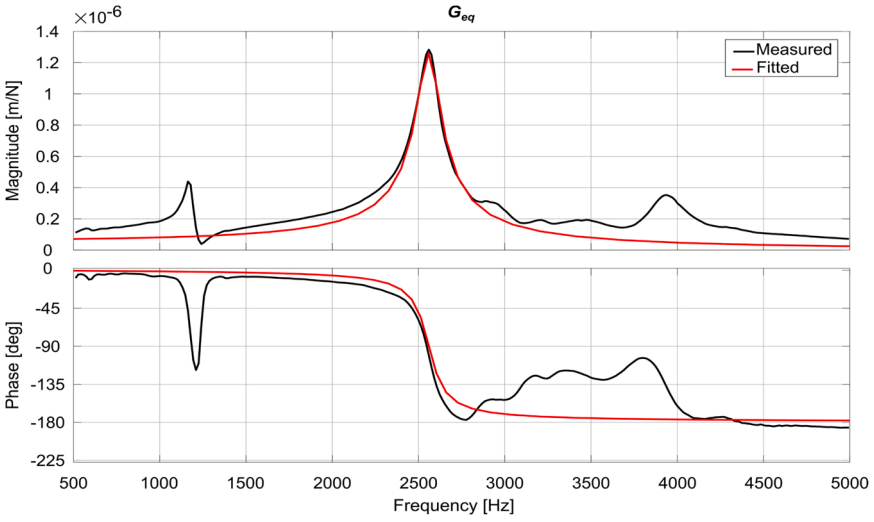

Fig. 15. Equivalent compliance of the setup.

Table 7
Experimental conditions for cutting.

Cutting conditions	
Spindle speed *SS*	1500–1800 [min^{-1}]
Cutting width b	0.5 – 1.25 [mm]
Static feed rate (static depth of cut) h_0	4.0 – 5.0 [μm/rev]
Tool modulation parameters	
Ratio of tool modulation frequency to spindle rotation frequency f_m/f_s	1.22–4.0
Tool modulation amplitude A	12.0–13.0 [μm]
Shift in tool trajectories in successive spindle revolutions ϕ	80–252 [deg]

Substituting 32(32) into 31(31) and combining with 30(30) allows prediction of successive tool tip position as:

$$y_d(t_{i+1}) = \frac{K_y b h_d(t_i) - m\left(\frac{-2y_d(t_i)+y_d(t_{i-1})}{\Delta T^2}\right) + c\frac{y_d(t_{i-1})}{2\Delta T} - k y_d(t_i)}{\frac{m}{\Delta T^2} + \frac{c}{2\Delta T}} \quad (33)$$

which is then used to calculate the dynamic uncut chip thickness in Eqs. (28) and (29). The occurrence of chatter is evaluated by running the simulation for a long period of time and manually judging the growth of tool vibrations. Considering the short duration of tool's in-cut phase, the simulation may have to be run for up to 200–500 spindle revolutions until considerable growth of chatter vibrations is observed and regenerative chatter condition is judged.

Before presenting the experimental results, a simulation study is conducted. Time domain simulations are conducted by using the specific cutting coefficients given in Table 5 and experimental system parameters given in Table 6 to demonstrate accuracy of the proposed stability solutions. For the semi-discrete time domain solution, the resolution of spindle revolution and width of cut are set to 1 rpm and 0.1 mm, respectively. The results are summarized in Fig. 10.

Firstly, it can be observed that MT provides significantly larger stable depth of (a_{lim}) as compared to conventional continuous turning. Time domain simulations are run to validate accuracy of the semi-discrete domain chatter stability predictions.

Fig. 10 presents some unique insight on the effect of phase angle and modulation frequency on the chatter stability as well. The left column of Fig. 10 shows stability when phase angle is fixed at $\phi = 180^0$ and modulation frequency is increased. As shown, increasing modulation

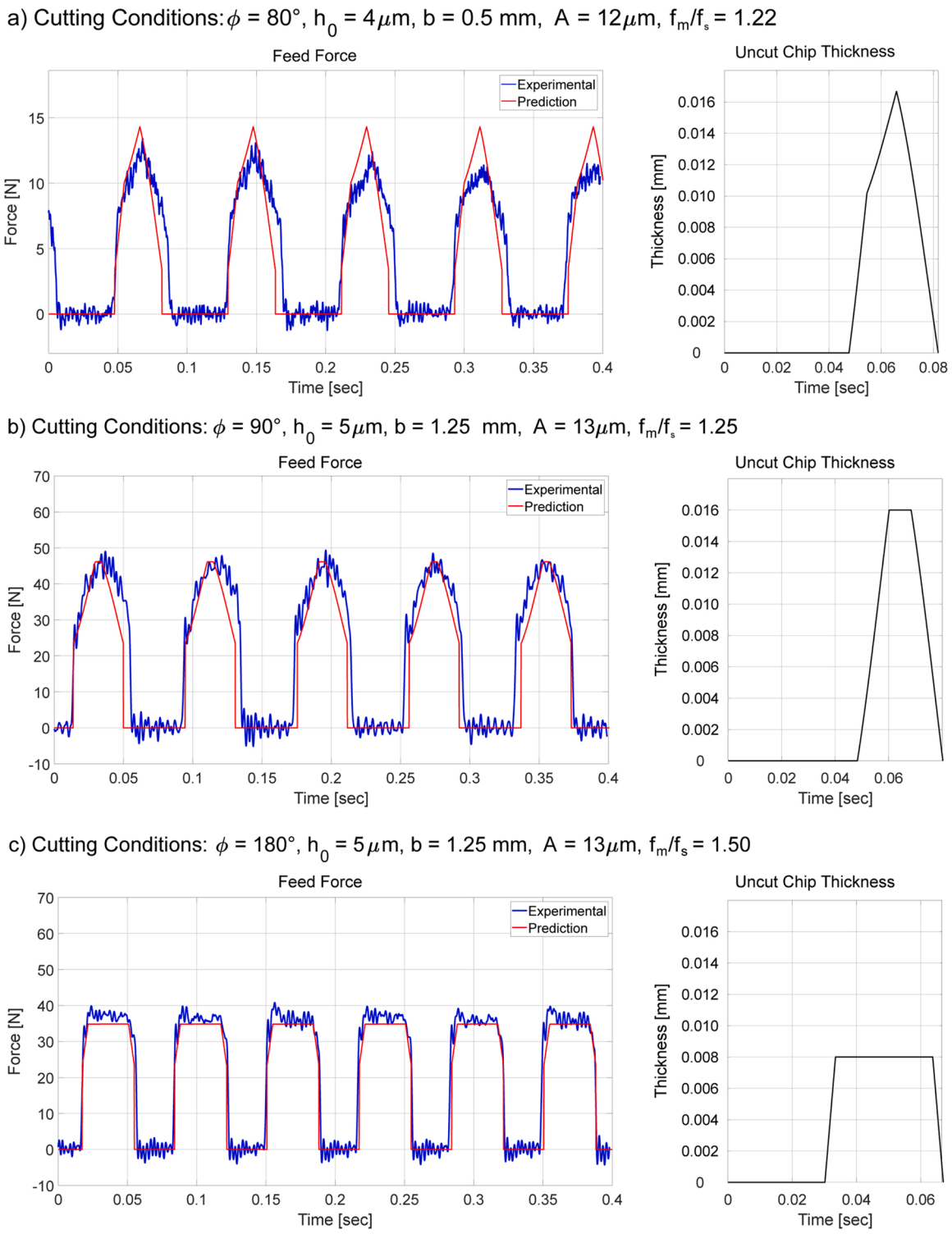

Fig. 16. Validation of cutting (feed/thrust) forces in various modulated turning conditions.

frequency stabilizes the system and directly increase the asymptotic stability border. For instance, at 1400[rpm] the stability is increased from 0.8[mm] up to ~1.2[mm] by increasing the modulation frequency by 6x (40[Hz] to 240[Hz]). Also note that increasing the spindle speed for a fixed modulation frequency increases overall stability limit as well. As compared to the stability lobes for continuous turning, stability lobes of MT are slightly tapered revealing stabilizing effect of spindle speed.

Right column of Fig. 10 presents effect of phase angle ϕ on the chatter stability. For a fixed modulation frequency-spindle frequency ratio $int(f_m/f_s)= 4$, phase angle is increased from $\phi = 90^0$ up to $\phi = 252^0$. As shown, the largest stability limit is observed for $\phi = 90^0$, and the lowest is observed when $\phi = 180^0$. The difference can be partially explained considering the air cutting duty ratio presented in Fig. 7. Note from Fig. 7 that for $\phi = 180^0$ the air cutting ratio is rather lowest, e.g. the tool is not cutting any workpiece roughly 35% of the spindle rotation period. In contrast, when $\phi = 90^0$, the air cutting ratio increases significantly. Noting from Fig. 7, it increases up to 45–50%. Since the tool spends longer time in air cutting, self-excited vibrations do not grow as fast.

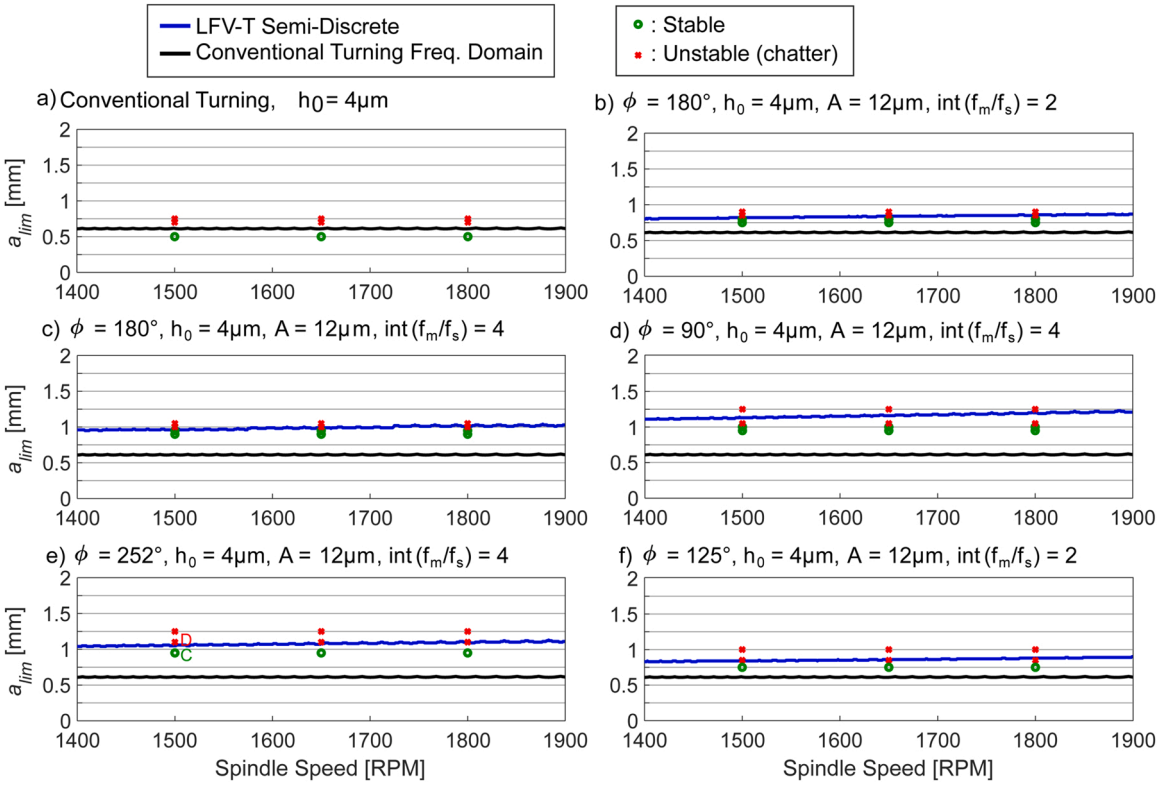

Fig. 17. Simulation and experimental results without/with tool modulation under various conditions.

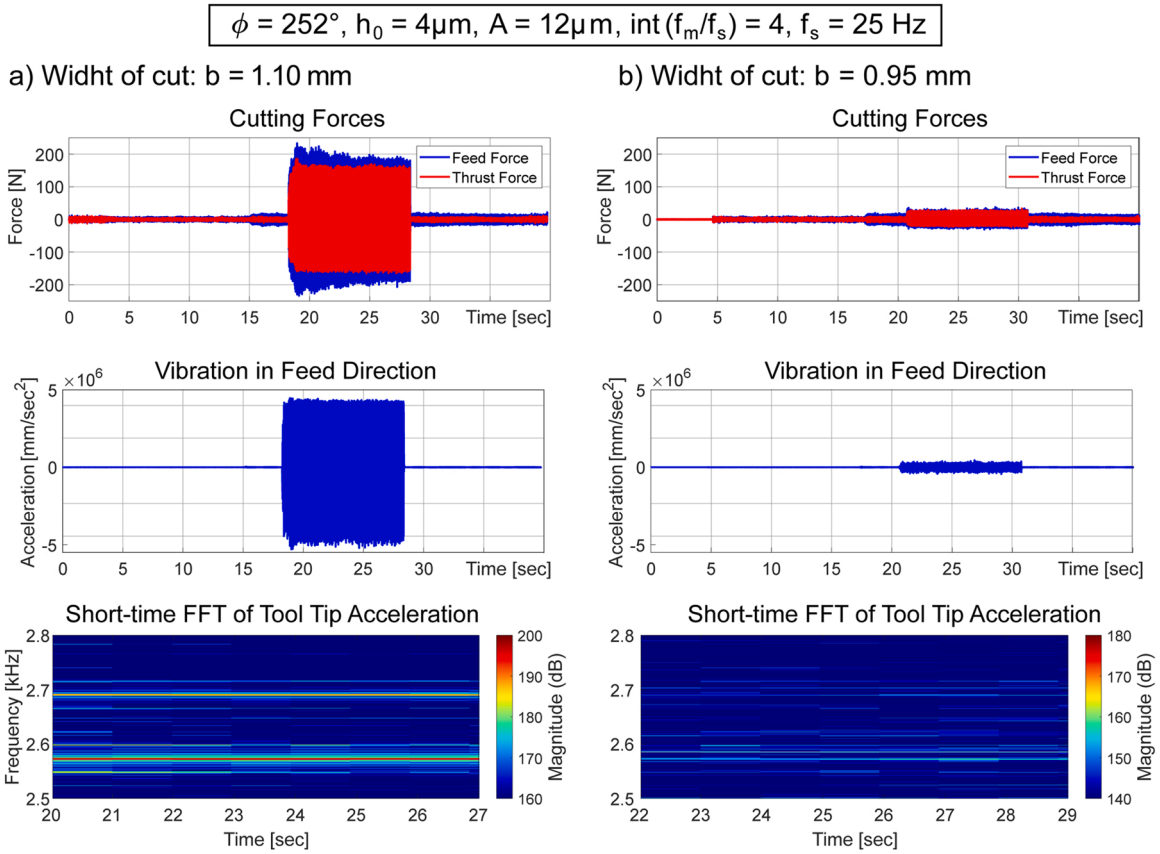

Fig. 18. Cutting signals recorded in stable and unstable cutting conditions (points C and D).

In Fig. 11, two of time domain analysis results, shown with "A" and "B" letters in Fig. 10-c, are given in detail. Here, two different widths of cut values are analyzed to compare stable and unstable conditions by using the same tool modulation parameters. As can be seen, for $b = 1.5$ mm, the process becomes unstable and chatter vibrations grow gradually. On the other hand, for $b = 0.8$ mm, process is stable and only forced vibrations can be observed. However, as shown in Fig. 11(d), slight vibration on chatter frequency is observed even for the stable case. This can be interpreted as follows. When width of cut is above the stability limit of the conventional cutting, chatter vibrations onset during in-cut (immersion) periods of the cutter. However, this in-cut period is too short for chatter growth, and the air-cutting (out-of-cut) region provides a dampening effect mitigating further growth of regenerative chatter.

4. Experimental validation

A series of experiments are conducted to verify the stabilizing effect by modulated turning and the validity of the stability solutions. The setup shown in Fig. 12 is used for experimental validation. Turning is realized on HAAS TL-1 CNC lathe, and tool is modulated in the feed direction using a piezo actuator driven fast tool servo (FTS) mounted on tool-post and controlled by a PID controller implemented in an in-house servo control system. Servo position loop is closed at 10 [kHz] sampling and positioning bandwidth is set to 300 [Hz]. Mechanical design and controller system of the FTS system are introduced in (Altintas and Woronko, 2002).

As shown in Fig. 12 Al6061 T6511 tubes with $d = 66.45$ [mm] diameter is used as workpiece material, and carbide insert with 7° relief angle is used as a cutting tool. Cutting forces are measured by a Kistler 9257B 3-axis dynamometer. A set of orthogonal cutting experiments are firstly conducted in stable cutting conditions to determine specific cutting force coefficients in feed/thrust (K_y) and principal (K_x) directions. The cutting width is set constant as 2.75 mm, and a various static feed rates are set from 2 μm/rev to 12 μm/rev considering the aimed modulation amplitude in cutting experiments. The gradient of each cutting force against the cross-sectional area of the uncut chip through linear fitting is identified as the specific cutting force. Fig. 13 shows the accuracy of the identification. Identified coefficients are given in Table 5.

Note that orthogonal tube-cutting experiments are conducted. Since material is removed on the face of the workpiece, it becomes very rigid in the feed direction (See Fig. 12). However, as shown in Fig. 12, the projection length of the tool shank is set long enough as 47 mm making it flexible in both feed (y) and principal (x) directions. In other words, the chatter mainly occurs on the tool side. Therefore, the dynamic compliance of the tool is measured by hammer testing on the tool tip. An impulse hammer (DYTRAN Instrument Inc., 5800SL 9083) is utilized for the force input, and two accelerometers (DYTRAN Instrument Inc., 3035B1 16021 and 3035B1G 15306) are utilized to measure the vibration acceleration in the two directions. The impact for each direction is repeated 15 times for higher reliability of measurement. It should be noted that the cutting force in feed (y) as well as in principal (x) directions affects vibration in the feed direction. Hence, the equivalent dynamic compliance (G_{eq}) [27] should be considered for the stability analysis. Fig. 14 shows the direct (G_{yy}) and cross (G_{yx}) dynamic compliances. The direct dynamic component (G_{yy}) is measured by exciting the tool tip in feed (y) direction and measuring its vibration in the same direction. Cross dynamic compliance (G_{yx}) is measured by exciting the tool in the principal (x) direction and measuring the vibration in the feed. The equivalent dynamic compliance (G_{eq}) can be calculated as:

$$G_{eq} = \frac{K_x}{K_y} G_{yx} + G_{yy} \tag{34}$$

Peak picking method (Altintas, 2011) is then used to identify modal parameters of G_{eq}, and fitting accuracy is shown in Fig. 15. As shown dominant resonance at 2.55 kHz is well represented by the model. Table 6 shows identified modal parameters.

Cutting experiments are carried out to validate the accuracy of cutting force prediction and the stability solutions. The experimental conditions for cutting are shown in Table 7. The pipe wall thickness of the workpiece is changed by pre-cut for setting the various cutting width. Beforehand of the actual cutting experiments, every actual tool modulation profile is validated against the reference profile to be certain with their accordance. Because of the limitation of the maximum amplitude and frequency of the piezo actuator, the tool modulation amplitude as well as the spindle speed are set a limited range as shown in Table 7.

Accuracy of cutting force prediction is firstly validated. Cutting tests are conducted in stable machining conditions. Note that the parameters of tool modulation in each cutting condition are set unequal to verify the influence of each modulation parameter into the accuracy of predicted cutting force. The tool modulation conditions and the results are presented in Fig. 16. The feed force is predicted by using the conventional orthogonal cutting model (Altintas, 2011) and compared with the experimental measurements. As shown in Fig. 16, the cutting forces are predicted accurately in all the condition. Specifically, the highest accuracy of predicted cutting force is confirmed at $\phi = 180°$ (Fig. 16-c). The reason for this result can be explained as follows. Due to static and dynamic deflections of the tool shank during cutting, in-cut and out-of-cut durations show small discrepancy [12]. In particular, the maximum cutting load at $\phi = 180°$ denotes smallest value because of its small uncut chip thickness as shown in Fig. 16-c, and hence the static and dynamic deflections of the tool shank comparatively smaller. In other words, the smallest delay between experimental and predicted force data is observed when the tool travels opposite to its trajectory in the previous revolution. Note that such delay from the static and dynamic deflection of the tool can influence chatter stability and it makes the small discrepancy between the predicted stability and the experimental results presented in the following.

Chatter tests with various tool modulation conditions are conducted to verify accuracy of predicted stability and to confirm the improved gained through MT compared to conventional turning process. Experimental results are summarized in Fig. 17. In order to evaluate the stability of the system, accelerometer signal in the feed direction is short-time Fourier transformed. As an indicator, the frequency domain vibration magnitudes are compared to the pre-determined tool modulation amplitude. The cases that show larger magnitude at a chatter frequency than the vibration magnitude at a modulation frequency are determined as unstable (chatter). Fig. 18 shows the experimental signals of cutting force, acceleration in feed direction, and its short-time Fourier transform results for both stable and unstable cases shown with "C" and "D" letters in Fig. 17-e.

As presented in Fig. 17, the proposed semi-discrete time domain solution accurately predicts the chatter stability of modulated turning for most cutting conditions. Some discrepancy is observed when $\phi = 90^0$, at which maximum chip thickness becomes 4x of the nominal feed rate. As discussed above, static deflection of flexible tool shank may distort the in-and-out-of-cut durations, may cause discrepancy between the simulated stability with the experimental results. On the other hand, the static deflection of the tool shank are the smallest at $\phi = 180°$, and hence the predicted stability shows a better accordance with experimental results as shown in Fig. 17-(b and c). It can be clearly confirmed that stability with tool modulation is higher than that of conventional turning process (without tool modulation) regardless of the tool modulation parameters. In particular, process stability is increased by more than 2x for $\phi = 90°$ and 252°. Although $\phi = 180^0$provides the smallest modulation frequency and amplitude conditions for implementation in practice [11], setting $\phi = 90^0$provides better stability. This is also discussed in previous section through simulation based benchmarks and summarized in Fig. 10. Next, the higher spindle speed with a certain tool modulation condition can achieve higher stability as shown in simulated solutions in each graph. Furthermore, as shown in Fig. 17-(b and c),

higher tool modulation frequency denotes the higher stability. The reason for this can be explained that a higher spindle speed/tool modulation frequency makes a shorter continuous in-cut section, and thus the chatter cannot be grown sufficiently even under the unstable condition.

5. Conclusion

This paper, for the first time, presented a generalized mechanics and dynamics model for the modulated turning (MT) processes.

Firstly, a generalized kinematic model is developed to predict the uncut-chip thickness. The developed model uses a tabulated approach to accurately model the complex chip formation observed in MT. It is found that a single chip consists of 3 sections (portions), and each portion is generated by the intersection of the current tool trajectory with the workpiece (undulated) surface generated in the multiple past spindle revolutions. The proposed approach can accurately describe the spindle revolutions involved in the generation of the undulated surface. Orthogonal cutting models are then applied to accurately predict the uncut chip thickness and resultant cutting forces.

The regenerative chatter stability of the process is also analyzed. Semi-discrete time approach is used and SLDs of the process are predicted. Accuracy of the stability predictions is validated both through time-domain simulations and via actual cutting experiments. It is observed that the proposed model can accurately estimate chatter stability of the modulated turning (MT) process. It is found that modulated turning can provide up to 2x higher chatter stability as compared to conventional single point continuous turning. It is clarified that stabilization effect of modulated turning originats from its discrete cutting kinematics and by the existence of the multiple regeneration loops.

CRediT authorship contribution statement

Bora Eren Role: Methodology, Experimentation, Formal analysis, Investigation, Writing – review & editing. **Soohyun Nam. Role**: Conceptualization, Experimentation, Writing – review & editing. **Burak Sencer Role**: Methodology, Experimentation, Formal analysis, Investigation, Writing – review & editing, Supervision, Project administration.

Declaration of Competing Interest

The authors declare that they have no known competing financial interests or personal relationships that could have appeared to influence the work reported in this paper.

Acknowledgement

This research is supported by the US's National Science Foundation (Award no: 2019370, GOALI/Collaborative Research: Mechanics and Dynamics of Low Frequency Vibration Assisted Machining).

References

Altintas, Y., 2011. Manufacturing Automation. Cambridge University Press. https://doi.org/10.1017/CBO9780511843723.

Altintas, Y., Stepan, G., Merdol, D., Dombovari, Z., 2008. Chatter stability of milling in frequency and discrete time domain. CIRP J. Manuf. Sci. Technol. 1 (1), 35–44. https://doi.org/10.1016/j.cirpj.2008.06.003.

Altintas, Y., Woronko, A., 2002. A piezo tool actuator for precision turning of hardened shafts. CIRP Ann. Manuf. Technol. 51 (1), 303–306. https://doi.org/10.1016/S0007-8506(07)61522-4.

Aoki, T., Sencer, B., Shamoto, E., Suzuki, N., Koide, T., 2016. Development of a high-performance chip-guiding turning process—tool design and chip flow control. Int. J. Adv. Manuf. Technol. 85 (1–4), 791–805. https://doi.org/10.1007/s00170-015-7990-5.

Chhabra, P.N., Ackroyd, B., Compton, W.D., Chandrasekar, S., 2002. Low-frequency modulation-assisted drilling using linear drives. Proc. Inst. Mech. Eng., Part B: J. Eng. Manuf. 216 (3), 321–330. https://doi.org/10.1243/0954405021519997.

Copenhaver, R., Schmitz, T., 2020. Modeling and simulation of modulated tool path (MTP) turning stability. Manuf. Lett. 24, 67–71. https://doi.org/10.1016/j.mfglet.2020.03.013.

Copenhaver, R., Schmitz, T., Smith, S., 2018. Stability analysis of modulated tool path turning. CIRP Ann. 67 (1), 49–52. https://doi.org/10.1016/j.cirp.2018.03.010.

Dombovari, Z., Munoa, J., Kuske, R., Stepan, G., Dombovari, Z., Munoa, J., Kuske, R., & Stepan, G. (2017). Non-smooth torus to identify domain of attraction of stable milling processes.

Eren, B., Sencer, B., 2020. Mechanistic cutting force model and specific cutting energy prediction for modulation assisted machining. Procedia Manuf. 48, 474–484. https://doi.org/10.1016/j.promfg.2020.05.071.

Gao, Y., Sun, R.L., Chen, Y.N., Leopold, J., 2016. Mechanical and thermal modeling of modulation-assisted machining. Int. J. Adv. Manuf. Technol. 86 (9–12), 2945–2959. https://doi.org/10.1007/s00170-016-8421-y.

Gao, Y., Sun, R., Leopold, J., 2018. An analytical force model for modulation-assisted turning. J. Manuf. Process. 31, 712–730. https://doi.org/10.1016/j.jmapro.2017.12.024.

Guo, Y., Lee, S.E., Mann, J.B., 2017. Piezo-Actuated modulation-Assisted drilling system with integrated force Sensing. J. Manuf. Sci. Eng. 139 (1), 38–45. https://doi.org/10.1115/1.4033929.

Guo, Y., Mann, J.B., Yeung, H., Chandrasekar, S., 2012. Enhancing tool life in high-speed machining of compacted graphite iron (CGI) using controlled modulation. Tribology Lett. 47 (1), 103–111. https://doi.org/10.1007/s11249-012-9966-z.

Hong, S.Y., Ding, Y., Ekkens, R.G., 1999. Improving low carbon steel chip breakability by cryogenic chip cooling. Int. J. Mach. Tools Manuf. 39 (7), 1065–1085. https://doi.org/10.1016/S0890-6955(98)00074-1.

Insperger, T., Stépán, G., 2004. Updated semi-discretization method for periodic delay-differential equations with discrete delay. Int. J. Numer. Methods Eng. 61 (1), 117–141. https://doi.org/10.1002/nme.1061.

Jawahir, I.S., van Luttervelt, C.A., 1993. Recent developments in chip control research and applications. CIRP Ann. 42 (2), 659–693. https://doi.org/10.1016/S0007-8506(07)62531-1.

Ma, C., Ma, J., Shamoto, E., Moriwaki, T., 2011. Analysis of regenerative chatter suppression with adding the ultrasonic elliptical vibration on the cutting tool. Precis. Eng. 35 (2), 329–338. https://doi.org/10.1016/j.precisioneng.2010.12.004.

Mann, J.B., Guo, Y., Saldana, C., Compton, W.D., Chandrasekar, S., 2011a. Enhancing material removal processes using modulation-assisted machining. Tribology Int. 44 (10), 1225–1235. https://doi.org/10.1016/j.triboint.2011.05.023.

Mann, J.B., Guo, Y., Saldana, C., Compton, W.D., Chandrasekar, S., 2011b. Enhancing material removal processes using modulation-assisted machining. Tribology Int. 44 (10), 1225–1235. https://doi.org/10.1016/j.triboint.2011.05.023.

Nam, S., Eren, B., Hayasaka, T., Sencer, B., Shamoto, E., 2021. Analytical prediction of chatter stability for modulated turning. Int. J. Mach. Tools Manuf. 165. https://doi.org/10.1016/j.ijmachtools.2021.103739.

Ozkirimli, O., Tunc, L.T., Budak, E., 2016. Generalized model for dynamics and stability of multi-axis milling with complex tool geometries. J. Mater. Process. Technol. 238, 446–458. https://doi.org/10.1016/J.JMATPROTEC.2016.07.020.

SAKURAI, K., ADACHI, K., OGAWA, K., 1992. Low frequency vibratory drilling of Ti-6Al-4V alloy. J. Jpn. Inst. Light Met. 42 (11), 633–637. https://doi.org/10.2464/jilm.42.633.

Uysal, E., Karaguzel, U., Budak, E., Bakkal, M., 2014. Investigating eccentricity effects in turn-milling operations. Procedia CIRP 14 (July), 176–181. https://doi.org/10.1016/j.procir.2014.03.042.

Yeung, H., Guo, Y., Mann, J.B., Compton, W.D., Chandrasekar, S., Dale Compton, W., Chandrasekar, S., Compton, W.D., Chandrasekar, S., 2016. Effect of low-frequency modulation on deformation and material flow in cutting of metals. J. Tribology 138 (1), 1–9. https://doi.org/10.1115/1.4031140.

Zhang, Y.Z., Peklenik, J., 1980. Chip curl, chip breaking and chip control of the difficult-to-cut materials. CIRP Ann. 29 (1), 79–83. https://doi.org/10.1016/S0007-8506(07)61299-2.

Zhu, L., Jiang, Z., Shi, J., Jin, C., 2015. An overview of turn-milling technology. Int. J. Adv. Manuf. Technol. 81 (1–4), 493–505. https://doi.org/10.1007/s00170-015-7187-y.